J. Fluid Mech. (1998), *vol.* 370, *pp.* 101–147. Printed in the United Kingdom

Low-frequency unsteadiness in the wake of a normal flat plate

By F. M. NAJJAR[1] AND S. BALACHANDAR[2]

[1] National Center for Supercomputing Applications, University of Illinois at Urbana-Champaign, Urbana, IL 61801, USA

[2] Theoretical and Applied Mechanics, University of Illinois at Urbana-Champaign, Urbana, IL 61801, USA

(Received 15 August 1997 and in revised form 21 April 1998)

The separated flow past a zero-thickness flat plate held normal to a free stream at $Re = 250$ has been investigated through numerical experiments. The long-time signatures of the drag and lift coefficients clearly capture a low-frequency unsteadiness with a period of approximately 10 times the primary shedding period. The amplitude and frequency of drag and lift variations during the shedding process are strongly modulated by the low frequency. A physical interpretation of the low-frequency behaviour is that the flow gradually varies between two different regimes: a regime H of high mean drag and a regime L of low mean drag. It is observed that in regime H the shear layer rolls up closer to the plate to form coherent spanwise vortices, while in regime L the shear layer extends farther downstream and the rolled-up Kármán vortices are less coherent. In the high-drag regime three-dimensionality is characterized by coherent Kármán vortices and reasonably well-organized streamwise vortices connecting the Kármán vortices. With a non-dimensional spanwise wavelength of about 1.2, the three-dimensionality in this regime is reminiscent of mode-B three-dimensionality. It is observed that the high degree of spanwise coherence that exists in regime H breaks down in regime L. Based on detailed numerical flow visualization we conjecture that the formation of streamwise and spanwise vortices is not in perfect synchronization and that the low-frequency unsteadiness is the result of this imbalance (or phase mismatch).

1. Introduction

Wakes of bluff bodies have been extensively studied because of their relevance to drag on vehicles, flow over ship hulls, and submarines. Such flows provide rich and interesting flow dynamics of considerable engineering relevance. Several basic geometrical configurations including circular and rectangular cylinders, flat plates, and airfoils have been experimentally and numerically investigated to understand the fundamental aspects of flow separation and wake instabilities. The normal flat plate is the simplest bluff body configuration that can be used to understand wake instabilities. Unlike the case of the circular cylinder, the flow past a flat place is characterized by fixed separation points at the edge of the plate. As a result, the wake behind a normal plate exhibits interesting complex dynamics even at modest Reynolds numbers.

There have been several previous experimental and numerical studies of flow past a flat plate placed in a uniform stream. Almost all of the experimental studies have been in the high-Reynolds-number regime from 1000 to 5×10^5 (Fage & Johansen 1927; Bradbury & Moss 1975; Perry & Steiner 1987; Steiner & Perry 1987; Kiya &

Matsumura 1988; Chua *et al.* 1990; Leder 1991; Lisoski 1993). Compared to the experimental studies, a relatively smaller number of numerical studies have been carried out for the flow past a normal flat plate. Earliest attempts are by Kuwahara (1973) and Kiya & Arie (1980) using the discrete-vortex method. Castro & Jones (1987) performed two-dimensional steady-state numerical simulations for Re in the range of 100 to 800. Because of the steady-state assumption, the length of the mean wake recirculation region was significantly over-predicted. These computations have since then been improved (Lisoski 1993) and extended to three dimensions (Joshi, Vanka & Tafti 1994; Najjar 1994; Najjar & Vanka 1995*a*; Najjar & Balachandar 1996).

A significant observation that can be made from the above studies (Lisoski 1993; Joshi *et al.* 1994; Najjar 1994; Najjar & Balachandar 1996) is that the temporal signal of drag and lift coefficients is marked by a strong component of low-frequency unsteadiness, over a wide range of Re from 250 to 2.5×10^5. The low frequency is about one tenth of the primary shedding frequency. The instantaneous drag coefficient can be observed to evolve back and forth between periods of high and low mean drag. This results in a low-frequency component superposed on the drag coefficient, in addition to its variation at twice the Kármán vortex shedding frequency. Owing to symmetry about the wake centreline, no such low-frequency component is superposed on the lift coefficient, which oscillates at the shedding frequency. On the other hand, the amplitudes of variation in both the drag and lift coefficients over a shedding cycle are significantly modulated by the low-frequency unsteadiness. In addition a low-frequency modulation of the shedding frequency can be observed.

In the canonical case of a circular cylinder, the presence of low-frequency unsteadiness is not so clear. Some of the earliest evidence of low-frequency unsteadiness can be found in the seminal work on cylinder wake by Roshko (1954). In the range $150 < Re < 300$, termed the transition range, irregular bursts appeared in the oscillograms with an approximate period of about 10 times the shedding period. Based on dye visualizations and velocity measurements at several points in the wake of a circular cylinder Tritton (1959) and later Berger (1964) observed two different modes of Kármán vortex shedding: a low-speed mode in the range $40 < Re < 110$ and a high-speed mode in the range $80 < Re < 160$. The low-speed and high-speed modes differed in their shedding frequency, and the transition between them was characterized by periodic beating, which was on the order of 6 to 14 times the primary shedding period. Subsequent experiments by Gaster (1969, 1971) raised the possibility that the discontinuity in the shedding frequency and the low-frequency beating are due to flow non-uniformities.

The effect of cylinder ends on the nature of Kármán vortex shedding was investigated by Gerich & Eckelmann (1982). They observed a central region of regular shedding frequency and affected regions, near the cylinder ends, characterized by a lower frequency. Above a certain critical Re low-frequency beatings were observed corresponding to the frequency difference between the central and the affected end zones. Recent computations by Dauchy, Dusek & Fraunie (1997) confirm the influence of the cylinder's free ends in generating a low-frequency beating even at Reynolds numbers as low as 54. Williamson (1992, 1996) observed that in the wake transition regime ($180 < Re < 260$), where mode-A instability gives way to mode-B instability, two different shedding frequencies coexist. The higher shedding frequency is associated with a more regular mode-B three dimensional state, whereas the lower shedding frequency is associated with large-scale vortex dislocations. He also observed that the two frequencies do not coexist, but the flow intermittently swaps between the states at a low frequency.

At Re in the range of 5×10^4 to 7×10^6, Schewe (1983) observed a strong low-frequency component in the time trace of drag and lift coefficients for a circular cylinder, qualitatively comparable to that observed for the normal plate by Lisoski (1993) and Najjar (1994). More recently Szepessy & Bearman (1992) and Szepessy (1994) have reported strong oscillations in the spanwise correlations of surface pressure measured on a circular cylinder near the separation line, having periods around 10 to 20 times the Strouhal period. The pressure correlation between different spanwise points also indicated that the low-frequency unsteadiness was associated with phase shifts, which he conjectured were similar to the natural vortex dislocations addressed by Williamson (1992).

On the computational front, Karniadakis & Triantafyllou (1992), Mittal & Balachandar (1995*a*) and Henderson (1994) at modest Reynolds numbers observed periods of almost periodic behaviour interspersed with periods of apparently random behaviour. These observations can be interpreted as a manifestation of low-frequency unsteadiness, but the time series were not long enough to be conclusive. Recent simulations by Belov, Jameson & Martinelli (1997) at $Re = 225$ showed the presence of a low-frequency component in the time trace of the lift coefficient and base pressure. While imperfect cylinder ends, as shown in experiments, can certainly lead to low-frequency beating even at very low Reynolds numbers, the observation of low-frequency unsteadiness in the three-dimensional simulations, where cylinder ends are avoided with an assumption of periodicity, suggests that low-frequency unsteadiness is an intrinsic property of the wake. Nevertheless, the observed amplitude of low-frequency unsteadiness has been so small that the low-frequency behaviour has not attracted much attention in the case of a circular cylinder.

Low-frequency unsteadiness has attracted significant attention in the context of separating-and-reattaching flows, such as flow past a backward-facing step (Eaton & Johnston 1982) and a blunt flat plate (Kiya & Sasaki 1983, 1985; Cherry, Hillier & Latour 1984). Here the primary imprint of low frequency is in the slow back and forth streamwise oscillation of the reattachment point. Eaton & Johnston (1982) suggested that the low-frequency unsteadiness is associated with a near two-dimensional vertical movement of the shear layer as a consequence of an instantaneous imbalance between the entrainment from the recirculation region along the shear layer and the reinjection of fluid near the reattachment point. Later measurements by Kiya & Sasaki (1985) confirmed this suggestion, but the amplitude of vertical oscillation was observed to be only 2.5% of the blunt flat plate's thickness. Cherry *et al.* (1984) associated the low-frequency unsteadiness with the characteristic time scale of relaxation between two different phases of shedding, and attempted to explain the cause of back and forth oscillation in the instantaneous reattachment point. Low-frequency unsteadiness was also observed in cavity flow (Rockwell & Naudascher 1979; Rockwell & Knisely 1980), primarily caused by the feedback of disturbances from the impingement point to the shear layer.

In spite of the above investigations, many aspects of the low-frequency behaviour still remain largely unexplored and unexplained. A detailed three-dimensional description of the process is in particular lacking. Here we will present results from a well-resolved direct numerical simulation of flow past a normal plate at $Re = 250$. Even at this modest Reynolds number, the drag and lift coefficients exhibit a strong low-frequency component and show striking resemblance to the corresponding high-Reynolds-number results (Najjar 1994; Lisoski 1993; Schewe 1983). Thus the wake of a normal plate at $Re = 250$ captures the essential features of low-frequency unsteadiness without the added complexities of a highly turbulent flow in the wake.

The present $Re = 250$ flow is by no means simple or regular; it is reasonably complex in order to support low-frequency unsteadiness, but simple enough to allow for detailed investigation of the instantaneous and phase-averaged vortical structures of the wake. It is observed that the low-frequency unsteadiness is primarily three-dimensional in nature and can be described as the process of flow gradually varying between two different states of three-dimensionality. These two three-dimensional states can be characterized by their coherence (or incoherence); the state of high mean drag is marked by reasonably regular spanwise and streamwise vortical structures, while the state of low mean drag is marked by spanwise vortices which are torn apart and an incoherent distribution of streamwise vortices. A simple filter has been developed to separately identify the spanwise and streamwise vortical structures, which allows evaluation of their individual statistics. Based on this, the three-dimensional states are characterized.

The paper is organized as follows. A brief discussion of the simulation details will be presented in §2. A detailed characterization of the low-frequency behaviour is presented in §3. To facilitate discussion, two distinctly different shedding regimes are defined: one corresponds to high mean drag, while the other corresponds to low mean drag. The details of the Kármán vortex formation and its dynamics within these two shedding regimes and their connection to the observed drag and lift behaviour are addressed in §4. A detailed discussion on the observed two different modes of three-dimensionality and statistics on spanwise and streamwise vortices in each of these modes is presented in §5. Section 6 presents a discussion of the present results in the context of other relevant observations and conjectures a possible physical mechanism for the observed low-frequency behaviour. Finally, §7 presents a brief conclusion.

2. Computational details

The time-dependent Navier–Stokes equations along with the incompressibility constraint are solved in three dimensions. All quantities are non-dimensionalized with the plate height (h_p) and the free-stream velocity (U_∞) as the length and velocity scales (see figure 1). The Reynolds number is then the only non-dimensional parameter, defined as $Re = h_p U_\infty/\nu$, where ν is the kinematic viscosity. The governing equations are discretized in time using a second-order-accurate, time-splitting procedure. The convective and diffusive terms are represented by a fully explicit Adams–Bashforth scheme. Although the explicit representation of the viscous terms requires a small time-step size at low Reynolds number, this restriction is somewhat eased at higher Reynolds numbers. The spatial discretization is accomplished with a high-order-accurate collocated finite-difference stencil along the streamwise (x) and cross-stream (y) directions. Along the spanwise direction (z) a Fourier discretization is used with a uniform distribution of points. Further details can be found in Najjar & Vanka (1995*b*), and Najjar (1994).

The computational domain extends from 5 non-dimensional units upstream of the normal plate in the streamwise direction (x) to 20 non-dimensional units in the downstream direction. In the cross-stream (y) direction it extends from $-L_y$ to $+L_y$, where $L_y = 8$. The spanwise width of the computation domain is chosen to be $L_z = 2\pi$ and a periodic boundary condition is used along the spanwise direction. This choice for the periodic spanwise extent was guided in part by the recent three-dimensional stability results for circular and square cylinders (Barkley & Henderson 1996; Williamson 1996; Robichaux, Balachandar & Vanka 1998). As will be seen below, the spanwise extent of the computational domain is large enough to accommodate from

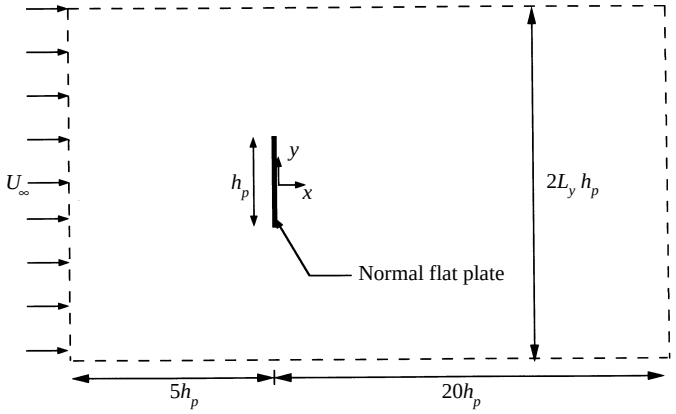

FIGURE 1. Schematic showing the normal flat plate and the extent of the computational domain. The origin of the coordinate system is fixed on the plate. The x-axis represents the downstream direction, the y-axis is cross-stream to the flow, and the z-axis is along the plate axis. The x, y grid resolution consists of 192×128 nodes. The mesh resolution in the spanwise direction is 48 nodes with a grid size of $2\pi/48 = 0.13$.

five to six pairs of three-dimensional streamwise (rib) vortical structures along the span and therefore is adequate in resolving all the spanwise flow variations. The present simulation at $Re = 250$ employed a grid of $192 \times 128 \times 48$ nodes along the streamwise, cross-stream and spanwise directions, respectively. In order to better resolve the near-wall flow features a smoothly varying non-uniform grid was used in the streamwise and cross-stream directions.

The following boundary conditions are applied along the edges of the computational domain: (i) At the inlet to the computational domain a uniform non-dimensional streamwise velocity of unity, and zero cross-stream and spanwise velocities are specified. Further, the normal gradient of pressure is set to zero in the solution of the pressure Poisson equation. (ii) At the top and bottom boundaries, free-stream conditions ($u = 1$, $p = v = w = 0$) are imposed. (iii) At the outlet of the computational domain, a convective boundary condition is applied. The effectiveness of the convective outflow boundary condition in the context of finite-difference methods has been addressed by Lowery & Reynolds (1986), Pauley, Moin & Reynolds (1990) and Najjar (1994). A convective velocity of 0.8 was chosen *a priori* based on the experiments of Kiya & Matsumura (1988). This was subsequently found to agree well with the convective velocity inferred from the current simulation. (iv) Along the spanwise direction a periodic boundary condition, $[\boldsymbol{u}(x, y, z, t) = \boldsymbol{u}(x, y, z + L_z, t)]$, was enforced. A thorough investigation of the effects of domain size, outflow boundary condition and grid resolution on the flow dynamics has been performed by Najjar (1994). In particular, it must be stressed that spurious resonant instabilities that can arise from outflow boundary conditions are not observed in the present simulation.

Results from a three-dimensional simulation at $Re = 250$ will be reported. The time-step size, Δt, is set to 4×10^{-3}, which maintains the convective (CFL) and diffusive numbers under their respective stability limits. The three-dimensional computation was started from the corresponding two-dimensional result with a random spanwise perturbation applied to the streamwise velocity in the vicinity of the plate for a brief period of 250 time steps to drive the flow into a three-dimensional shedding state. The saturation of the three-dimensional mode has been monitored by following the volume-integrated streamwise vorticity magnitude ($\Omega = \int\int\int |\omega_x| \mathrm{d}x\, \mathrm{d}y\, \mathrm{d}z$), shown in

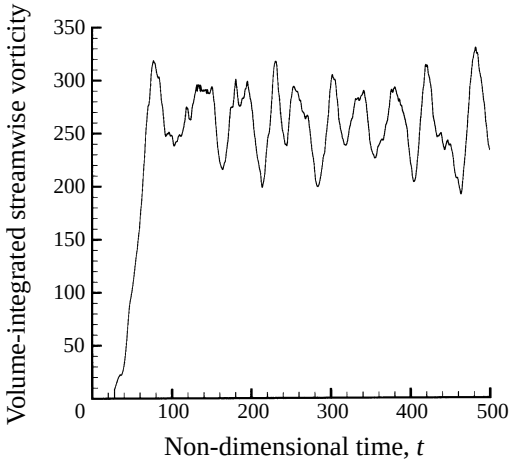

FIGURE 2. Transition from a two-dimensional flow to a three-dimensional flow is monitored with the temporal signature of the volume-integrated streamwise vorticity magnitude, $\int\int\int |\omega_x| \, \mathrm{d}x \, \mathrm{d}y \, \mathrm{d}z$. The flow is fully three-dimensional by about $t = 100$.

figure 2. This quantity provides a sensitive measure of three-dimensionality and in particular three-dimensional vortical structures (Mittal & Balachandar 1995*a*). Ω is identically zero in the two-dimensional state and with the introduction of three-dimensionality it initially increases exponentially due to linear instability. The saturation of three-dimensionality by nonlinear mechanisms is characterized by the levelling-off of Ω, which in figure 2 occurs after around 80 non-dimensional units. The quasi-periodic oscillation of Ω is indicative of the chaotic nature of the saturated three-dimensional shedding state. The simulation was integrated further for up to 512 non-dimensional time units. At this *Re* we observe an average shedding period of 6.5 non-dimensional time units, hence the present computation spans approximately 66 shedding cycles. The computations were performed on the massively parallel CM5 and the entire simulation required approximately 500 CPU hours on a 128 node partition. The pressure and three-dimensional velocity fields have been stored every hundred time steps (0.4 time units) thus providing approximately 16 flow dumps every shedding cycle. These dumps are processed *a posteriori* to compute time and phase-averaged flow structures which will be discussed in detail in the following sections.

3. Shedding and low-frequency components of drag and lift

3.1. *Comparison of two- and three-dimensional simulations*

Figures 3(*a*) and 3(*b*) illustrate the temporal variation in the instantaneous drag coefficient, C_D, as computed from two- and three-dimensional simulations, respectively. In the case of the three-dimensional simulation, the drag coefficient is based on the span-averaged drag force on the normal plate. As observed by many earlier investigators (for example, Najjar & Vanka 1995*a*; Mittal & Balachandar 1995*a*; Chua *et al.* 1990; Tamura, Ohta & Kuwahara 1990) the two-dimensional simulation considerably overpredicts the drag coefficients with a mean C_D of 3.36. The mean drag coefficient predicted by the three-dimensional simulation is 2.36. Thus, even at the present low Reynolds numbers of $Re = 250$, restriction to two-dimensionality results in an approximately 42% overprediction of mean drag. The drag coefficient computed in the three-dimensional simulation is somewhat larger than the range of experimentally

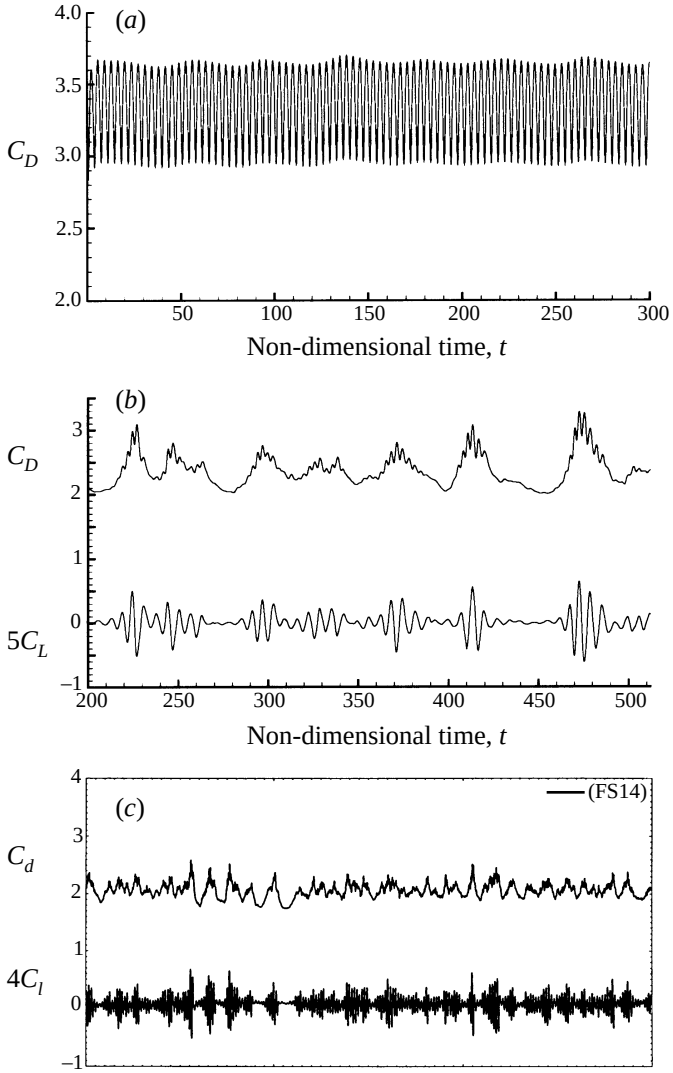

FIGURE 3. Time variation of (*a*) the drag coefficient obtained from the two-dimensional simulation, (*b*) the drag and lift coefficients obtained from the three-dimensional simulation, (*c*) experimental results of Lisoski (1993) at $Re = 6000$. The drag coefficient oscillates at twice the Kármán shedding frequency. The two-dimensional simulation captures a periodic drag variation with a primary non-dimensional shedding period of 3.6. The shedding period obtained in the three-dimensional simulation is about 6.2. Also in the experiment and in the three-dimensional simulation a strong low-frequency unsteadiness can be seen.

measured value of 1.8 to 2.15 (Fage & Johansen 1927; Abernathy 1962; Castro 1971; Arie & Rouse 1956; Lisoski 1993). However, the Reynolds number of these experiments is generally much larger and furthermore if blockage and leakage effects are accounted for (Abernathy 1962 and Maskell 1963) then the corrected experimental and computational drag coefficients approach each other.

The fundamental difference between the two- and three-dimensional simulations is brought out well in the corresponding instantaneous contours of spanwise vorticity (ω_z) shown in figures 4(*a*), 4(*b*) and 4(*c*). In the case of the three-dimensional simulation, contours of the span-averaged spanwise vorticity are plotted on the (x, y)-

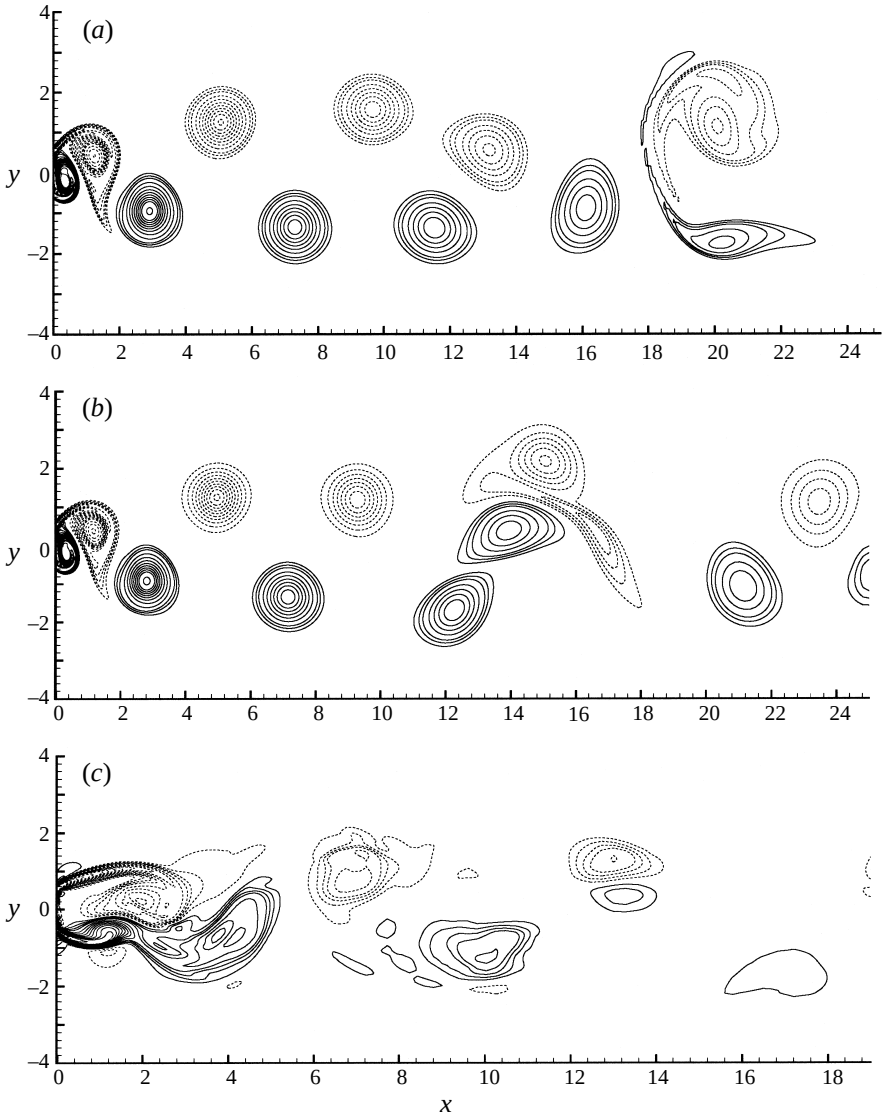

FIGURE 4. Contour plots of instantaneous spanwise vorticity, ω_z, in the near wake of the normal flat plate computed from (a, b) two-dimensional simulation at two different times, (c) three-dimensional simulation. Span-averaged values are presented in the case of the three-dimensional computation. Dashed (solid) contours represent clockwise (counterclockwise) rotation. Three sets of contour levels are used: (± 0.25 to ± 1.0 in steps of 0.25), (± 1.0 to ± 5.0 in steps of 0.5) and (± 5.0 to ± 10.0 in steps of 1.0).

plane. The first striking difference is in the structure of the shear layers developing from the edges of the plate located at $y = \pm\frac{1}{2}$ and $x = 0$. In the three-dimensional simulation, the shear layer is seen to extend downstream up to two plate heights before roll-up into Kármán vortices. In two dimensions, the shear layers roll-up much closer to the plate. Further, in the three-dimensional simulation, the vortices can be seen to break-up into smaller vortices farther downstream for $x > 8$, whereas in the two-dimensional simulation the Kármán vortices undergo no such break-up; they remain strong and distinct and maintain their coherence as they convect parallel to the centreline.

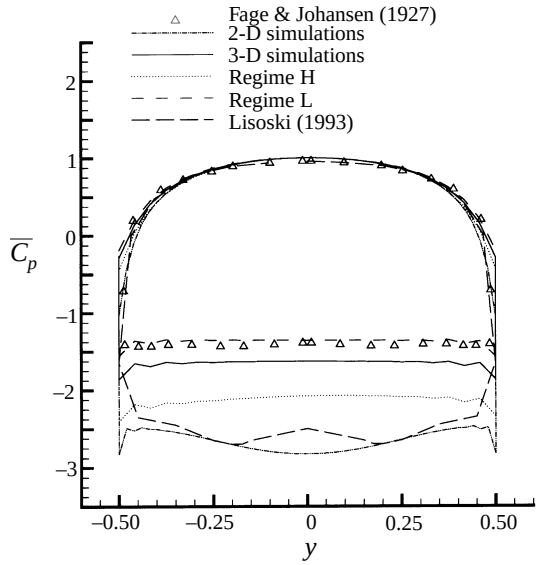

FIGURE 5. Distribution of the mean pressure coefficient, $\bar{C}_p$, along the plate surface obtained from experiments and computations. The experimental data of Fage & Johansen (1927) and for $Re = 1.5 \times 10^5$ and the computational results of Lisoski (1993) are obtained from a two-dimensional discrete-vortex method. Both current two-dimensional and three-dimensional results are presented. Also shown are the distributions of mean pressure coefficient obtained by time integration only within regimes H and L of the present three-dimensional simulation.

Occasional interaction between the vortices can be observed for $x > 12$. For example, in figure 4(*a*) the clockwise and anticlockwise vortices that are about to exit the computational domain can be seen to strongly interact at $x = 20$. While at another instant in time shown in figure 4(*b*), the Kármán vortices exiting the computational domain do not exhibit strong interaction, upstream Kármán vortices at $x = 15$ show strong interaction. Nevertheless, the absence of three-dimensionality in the form of vortex stretching and tilting preserves the form of these spanwise vortices without much distortion.

The compact vortices that form closer to the normal plate in the two-dimensional simulation are responsible for the higher suction pressure along the base and result in a significantly higher drag. This can be seen in figure 5, where the distribution of the mean pressure coefficient, $\bar{C}_p = 2(\bar{p}^* - p^*_\infty)/(\rho U^2_\infty)$, based on the time- and span-averaged dimensional pressure, $\bar{p}^*$, is plotted around the surface of the plate. In terms of the computed non-dimensional mean pressure distribution, $\bar{p}$, the pressure coefficient can be written as $\bar{C}_p = 2(\bar{p} - p_\infty)$. Also presented are the experimental data of Fage & Johansen (1927) and the computational results of Lisoski (1993) using the discrete-vortex method. The current three-dimensional simulation compares well with the experimental data, whereas the two-dimensional as well as the discrete-vortex simulations predict a significantly lower base pressure and do not capture the 'flat' distribution of pressure on the back side of the plate. The near constant pressure in the base region, measured in the experiments is, however, well captured by the three-dimensional simulation. The non-uniform pressure distribution along the base and the higher suction have been observed in the two-dimensional simulation of other bluff body geometries as well (Mittal & Balachandar 1995*a*; Tamura *et al.* 1990).

In the two-dimensional simulation (figure 3*a*), the drag coefficient exhibits a

dominant periodic time variation with a period of about 3.6 non-dimensional time units driven by the Kármán vortex shedding process in the wake. This translates to a primary two-dimensional shedding period of 7.2, since the drag coefficient oscillates at twice the shedding frequency. Apart from this dominant frequency, a low-amplitude low-frequency unsteadiness can also be observed to be superimposed on the drag variation. This low-frequency unsteadiness appears to occur with a period of about 10 times the fundamental period of drag variation or 5 times the period of the Kármán vortex shedding process.

Oscillations at twice the shedding frequency can be observed in the instantaneous span-averaged drag signature of the three-dimensional simulation as well (see figure 3*b*); however, the amplitude of drag oscillation at this frequency is greatly diminished. The overprediction of fluctuation in the drag coefficient at twice the shedding frequency, observed in the two-dimensional simulation, is consistent with earlier findings in other bluff body geometries (Mittal & Balachandar 1995*a*). Also plotted in figure 3(*b*) is the corresponding variation in the instantaneous span-averaged lift coefficient, C_L, computed in the three-dimensional simulation. For a normal plate of zero thickness, at zero angle of attack the pressure distribution around the plate contributes only to the drag force. The instantaneous lift force is solely due to the net y viscous shear on the front and back sides of the plate. The vertical (or y) viscous shear stress on the plate can be expressed in terms of the non-dimensional spanwise vorticity as $\mu U_\infty \omega_z/h_p$. The instantaneous coefficient of lift can then be expressed in terms of the non-dimensional spanwise vorticity distribution around the plate as

$$C_L = \frac{2}{Re}\left[\int_{-1/2}^{1/2} (\omega_{z,Back} - \omega_{z,Front})\,\mathrm{d}y\right],$$

where $\omega_{z,Front}$ and $\omega_{z,Back}$ define spanwise vorticity on the front and back faces of the normal plate. The mean period of vortex shedding observed in the lift coefficient is $T_p = 6.2$, corresponding to a primary shedding (or Strouhal) frequency of $F_p = 1/T_p = 0.16$. Thus, restriction to two-dimensionality results in not only overprediction of the mean and fluctuating drag and lift forces, but also a 16% overprediction of the primary vortex shedding period.

The drag and lift coefficients reveal a strong component of unsteadiness at a much lower frequency with a long period of approximately ten times that of the main vortex shedding process. The nature of low-frequency unsteadiness observed in the three-dimensional simulation appears to be significantly different from that observed in the two-dimensional simulation. The low-frequency component in the two-dimensional simulation is due to the Kármán vortex interaction process seen in figures 4(*a*) and 4(*b*). Such interaction occurs every five shedding cycles or so, thus explaining the observed low-frequency component in the drag coefficient (see figure 3*a*). The Kármán vortex interaction can be clearly observed only sufficiently downstream of the normal plate for $x > 10$ and as a result the amplitude of the low-frequency component in figure 3(*a*) is significantly smaller than that at twice the shedding frequency. In contrast, in the three-dimensional simulation the variation in drag coefficient is significantly stronger at the low frequency than at twice the shedding frequency.

In three dimensions, the Kármán vortices do not exhibit the same kind of periodic interaction as observed in two dimensions. The physical mechanism responsible for the low-frequency unsteadiness observed in the three-dimensional simulation is distinctly different from that at work in the two-dimensional simulation and as will be demonstrated below it relies upon the different modes of three-dimensional instabilities. The difference is quite evident in the drag signature shown in figures 3(*a*) and 3(*b*). In

figure 3(*a*) the low frequency can be considered as a simple superposition on the shedding process, whereas in figure 3(*b*) apart from superposition, the low frequency also modulates both the amplitude and frequency of the shedding process.

A three-dimensional simulation at a higher Reynolds number of $Re = 1000$ also displays a similar strong low-frequency component in the drag and lift signatures (Najjar & Vanka 1995*a*). It is important to point out that the temporal variation of drag and lift coefficients shown in figure 3(*b*) closely resembles the experimental measurements of C_D and C_L by Lisoski (1993) shown in figure 3(*c*) for $Re = 6000$. For the case of a circular cylinder, similar behaviour for drag and lift coefficients can be observed in the experimental results of Schewe (1983) over a high-Reynolds-number range of 5×10^4 to 7×10^6 (see his figures 13 and 14). Similar low-frequency unsteadiness has also been observed in the context of separating-and-reattaching flows (Eaton & Johnston 1982; Kiya & Sasaki 1983, 1985; Cherry *et al.* 1984).

3.2. *Characterization of low-frequency unsteadiness*

Even at the modest Reynolds number of $Re = 250$, the wake dynamics as predicted in the present three-dimensional simulation is quite complex and the resulting drag and lift variations as shown in figure 3(*b*) are fairly irregular. However, the primary shedding and low-frequency components appear to dominate the essentially chaotic behaviour. In the case of the lift coefficient, C_L, its variation to first approximation can be adequately represented as a low-frequency modulation of lift variation at the primary shedding frequency. The lift variation can then be approximately expressed as: $a_L \sin^2(\pi F_s t) \sin(2\pi F_p t + \phi_L)$, where ϕ_L is the phase angle between the primary shedding and low-frequency modulation processes. Here a_L represents the amplitude of the low-frequency modulated lift variation. The shedding (primary) and secondary low frequencies are denoted by F_p and F_s, respectively.

In the case of the drag coefficient, a low-frequency component can be clearly identified. The mean drag evaluated over each shedding cycle can be observed to vary between 2 and 3. Although not as clear as in the lift variation, a low-frequency modulation of the drag coefficient can also be identified. The amplitude of drag variation over a shedding cycle is large when the mean drag is large (at $t \approx 225$, 250, 300 and 375), whereas when the mean drag is low, variation in drag coefficient over a shedding cycle is nearly absent (at $t \approx 210$, 275 and 350). The drag variation can be approximately expressed as: $\bar{C}_D + a_{D1} \sin^2(\pi F_s t) \sin(4\pi F_p t + \phi_D) - a_{D2} \cos(2\pi F_s t)$, where $\bar{C}_D$ is the time-averaged mean drag coefficient and ϕ_D is the phase angle. Here a_{D1} and a_{D2} represent the amplitudes of the contribution to the drag coefficient from the modulated shedding process and the low-frequency unsteadiness, respectively. The amplitude of the low-frequency component, a_{D2}, is observed to be larger than the amplitude of modulated shedding process, a_{D1}. In comparison, in the two-dimensional simulation (figure 3*a*) the low-frequency modulation of the shedding process is virtually non-existent, and the low-frequency contribution to the drag coefficient is at a relatively low amplitude.

A careful examination of the drag and lift coefficients plotted in figures 3(*b*) and 3(*c*) shows that not only the amplitude but also the shedding frequency is significantly modulated by the low-frequency unsteadiness. This frequency modulation is more evident in figure 6 which shows a close-up of the time history of the drag and lift coefficients spanning 100 non-dimensional time units from $t = 412$ to 512, covering approximately two low-frequency periods. To quantify the amplitude and frequency modulations, the beginning of each Kármán shedding cycle is arbitrarily defined by the local peak value of C_L. Thus shedding cycles are defined to extend between adjacent

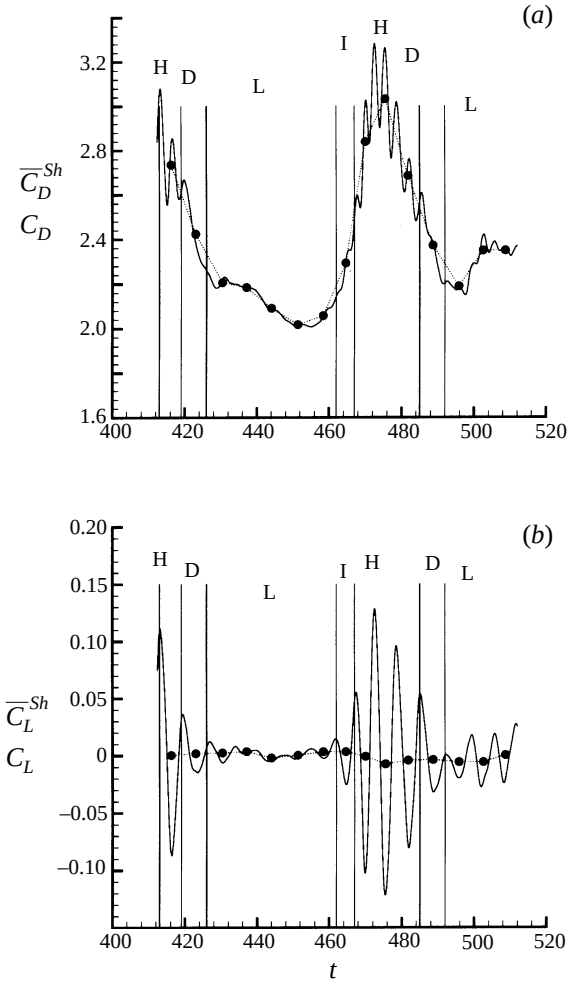

FIGURE 6. Modulation of (*a*) the drag and (*b*) lift coefficients during the time period extending from $t = 412$ to 512 covering two low-frequency cycles. Four regimes are identified and are denoted as the regime of high drag (marked H), the regime of low drag (marked L), the regime of increasing drag (marked I), and the regime of decreasing drag (marked D). Their temporal extents are demarcated by the vertical lines. The mean drag and lift coefficients averaged within each shedding cycle, $\bar{C}_D^{Sh}$ and $\bar{C}_L^{Sh}$, are plotted as (⋯ ● ⋯).

peaks in the lift coefficient. For each shedding cycle, the shedding period, T_p, the mean coefficients of drag and lift, $\bar{C}_D^{Sh}$ and $\bar{C}_L^{Sh}$, and amplitudes of drag and lift variation, a_D^{Sh} and a_L^{Sh}, are computed. The amplitudes of drag and lift variation are simply defined as half the difference between the maximum and minimum values of the drag and lift coefficients, respectively, during that cycle.

In figure 6(*a*) overlaid on the drag coefficient is a plot of $\bar{C}_D^{Sh}$ versus t, where the time for each shedding cycle is taken to be at the mid-point of the cycle. By definition, the time variation in C_D captured by $\bar{C}_D^{Sh}$ accounts for only the contribution to the drag coefficient from the low-frequency component and the difference between C_D and $\bar{C}_D^{Sh}$ is due to the Kármán vortex shedding process. Thus the temporal variation in $\bar{C}_D^{Sh}$ shows an approximately sinusoidal behaviour arising from the low-frequency unsteadiness, whose amplitude provides an estimate for a_{D_2} of about 0.5.

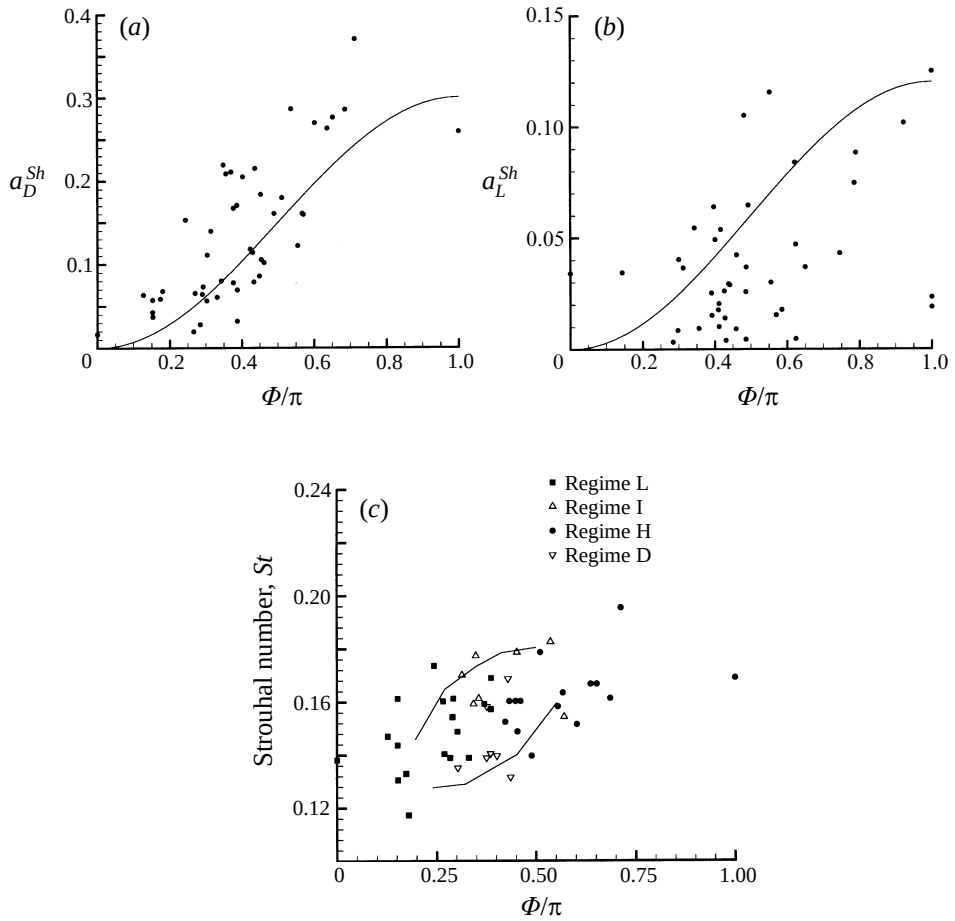

FIGURE 7. Distribution of (*a*) the amplitude of the drag oscillation, a_D^{Sh}, (*b*) the amplitude of the lift oscillation, a_L^{Sh}, and (*c*) the shedding frequency, against the phase along the low-frequency cycle, Φ. $\Phi = 0$ and 2π correspond to time instants of low drag and $\Phi = \pi$ corresponds to time instants of high drag. Analytical models of the amplitudes of drag and lift coefficient variation within each shedding cycle are presented as solid lines: (*a*) $a_{D1}\sin^2(\Phi/2)$ with $a_{D1} = 0.3$, (*b*) $a_L\sin^2(\Phi/2)$ with $a_L = 0.12$. In the distribution of shedding frequency, data from the four different regimes are marked by four different symbols. A possible hysteresis in shedding frequency between increasing and decreasing phase of low-frequency unsteadiness is sketched as two solid lines in (*c*). A general trend of higher shedding frequency with increasing mean drag can be identified in (*c*).

Each cycle of low-frequency unsteadiness is arbitrarily defined to extend between two adjacent minima of $\bar{C}_D^{Sh}$ (from one point of minimum $\bar{C}_D^{Sh}$ to the next). Based on this definition, at any time instance the corresponding phase during the low-frequency cycle can be defined as

$$\Phi = \cos^{-1}\left(\frac{2(\bar{C}_D^{Sh} - \bar{C}_D)}{(\bar{C}_{D,max}^{Sh} - \bar{C}_{D,min}^{Sh})}\right). \tag{1}$$

The time-averaged mean drag coefficient, $\bar{C}_D = 2.36$, is also the average of $\bar{C}_D^{Sh}$ over many low-frequency cycles. Further, $\bar{C}_{D,min}^{Sh}$ and $\bar{C}_{D,max}^{Sh}$ are the minimum and maximum of $\bar{C}_D^{Sh}$ and therefore the denominator is approximately given by $2a_{D2}$. With the above definition, the low-frequency phase can be computed at any given time and

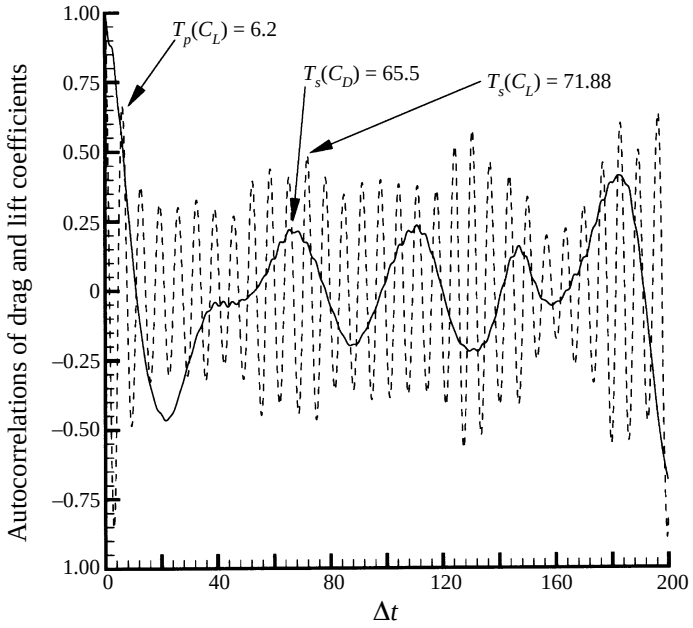

FIGURE 8. Autocorrelations of drag and lift coefficients are represented by solid and dashed lines respectively. The dominant peak in the autocorrelation of lift corresponds to a shedding period of about 6.2, while the dominant peak in the drag coefficient corresponds to low-frequency period of about 65.5. The peak corresponding to the low-frequency unsteadiness in the lift coefficient suggests a slightly longer period of about 71.88.

it is in the range $0 \leqslant \Phi \leqslant 2\pi$. The low-frequency phases, $\Phi = 0$ and 2π, correspond to time instances of overall low drag ($\bar{C}_D^{Sh} \to \bar{C}_{D,min}^{Sh}$), while $\Phi = \pi$ corresponds to instances of high drag ($\bar{C}_D^{Sh} \to \bar{C}_{D,max}^{Sh}$).

The amplitude and frequency modulation of the shedding process by the low-frequency unsteadiness can now be extracted by plotting the shedding period, T_p, and the amplitudes of drag and lift variation, a_D^{Sh} and a_L^{Sh}, over each shedding cycle against the corresponding phase, Φ, along the low-frequency cycle. In figures 7(*a*) and 7(*b*), a_D^{Sh} and a_L^{Sh}, for 47 different shedding cycles are plotted against the low-frequency phase (computed from equation (1)) at the mid-point of the shedding cycle. Also plotted is the approximate form of the low-frequency modulation of drag and lift coefficients: $a_{D1}\sin^2(\Phi/2)$ and $a_L\sin^2(\Phi/2)$. The scatter in the data points is indicative of the chaotic nature of the shedding and low-frequency processes, which is quite evident from the time history of drag and lift coefficients (see figure 3). Nevertheless the data points show the same qualitative trend as the analytical expression. The approximate amplitudes of drag and lift modulation can be estimated from these figures as $a_{D1} = 0.3$ and $a_L = 0.12$, respectively. Thus it can be seen that drag variation due to low-frequency unsteadiness ($2a_{D2}$) is about 67% larger than drag variation due to the shedding process ($2a_{D1}$).

Figure 7(*c*) shows variation in the primary shedding frequency ($F_p = 1/T_p$) against the corresponding low-frequency phase for 47 shedding cycles. A general trend of higher shedding frequency (or lower shedding period) with increasing mean drag ($\Phi \to \pi$) can be identified. Extraction of an exact form for this frequency modulation is made difficult by the scatter in the plot, but significant variation in shedding frequency from about 0.12 to 0.18 can be observed. The data points in this figure are marked by four

different symbols: filled squares indicate shedding cycles during which the mean drag was low; up-triangles indicate shedding cycles during which the mean drag is on the rise; filled circles correspond to cycles of high mean drag; and finally down-triangles correspond to cycles of decreasing mean drag (more precise classification will be provided below). In addition to the general trend of increasing shedding frequency with increasing phase (or mean drag), as indicated in the plot, a tendency towards hysteresis can also be identified.

It must be cautioned that the functional forms presented above for the drag and lift coefficients are intended to serve only as a model, since the actual low-frequency effect neither simply superposes nor simply modulates the Kármán vortex shedding process. Significant nonlinear interaction exists between the mechanisms responsible for Kármán vortex shedding and low-frequency unsteadiness resulting in a chaotic wake dynamics. The complex nature of low-frequency unsteadiness is clear from the fact that that its period does not remain fixed. It can be observed that the low-frequency period varies anywhere between 35 and 55 non-dimensional time units. Furthermore, the low-frequency unsteadiness appears to be asymmetric, resulting in relatively longer duration of quiescence and low mean drag separated by comparatively shorter duration of intense vortex shedding and high mean drag. Such asymmetry in the low-frequency unsteadiness was originally suggested by Eaton & Johnston (1982). Based on surface pressure measurements Kiya & Sasaki (1985) have estimated the time duration of low drag to extend nearly twice as long as that of high drag in a reattaching flow over a blunt plate. These observations are consistent with the behaviour of the drag coefficient shown in figure 3(*b*). Thus the strength of the shedding process appears to influence the nature of the low-frequency unsteadiness as well.

3.3. *High, low and transition drag regimes*

A simple physical interpretation of the low-frequency behaviour seen in the drag and lift variations is that the flow periodically varies between two extreme states: an active state of strong vortex shedding marked by large-amplitude oscillation in drag and lift and a weak vortex shedding state marked by low levels of drag and lift variation. The existence of such distinctly different shedding states has been previously inferred based on experimental measurements by Kiya & Sasaki (1985). As remarked above, the total duration of these states need not be equal and the frequency of Kármán vortex shedding is significantly higher in the active state than in the relatively weaker state. Based on the close-up shown in figure 6, four different flow regimes have been identified as follows:

(i) The *high-drag regime* (marked H) encompasses the time interval where the drag coefficient is large and the corresponding lift coefficient shows large fluctuations. In figure 6 this occurs over the following time intervals: $t = 413$–419 and $t = 467$–485.

(ii) The *low-drag regime* (marked L) represents the time interval where the drag coefficient is low with a correspondingly low level of fluctuation in the lift coefficient. This regime is observed to occur for $t = 426$–462 and $t > 492$.

(iii) The *transition regimes* (marked D and I) represent the transition regimes that link regimes H and L. Regimes D and I represent regions with decreasing and increasing drag coefficient, respectively. In figure 6 the time frames during which these transitions occur at $t = 419$–426, $t = 485$–492 and $t = 462$–467.

Autocorrelations of the drag and lift coefficients computed over the entire period are shown in figure 8. The shedding period of $T_p = 6.2$ is well captured by the dominant peak in the autocorrelation of lift, while the influence of the shedding process is seen to have only a weak effect on the autocorrelation of drag. The dominant peak in the

drag correlation corresponds to a low-frequency period of $T_s = 65.5$. Thus the low-frequency unsteadiness of the wake is at about one tenth of the shedding frequency. This ratio between the shedding and low frequencies is an agreement with the experimental measurements of Lisoski (1993) for the flow over a normal plate and with the spectral simulation results of Henderson (1994) for flow over a circular cylinder. In the case of a separating-and-reattaching flow over a blunt flat plate Kiya & Sasaki (1985) observe a low frequency of 1/6th the shedding frequency. Other measurements (Roshko 1954; Tritton 1959; Gerich & Eckelmann 1982; Williamson 1992; Szepessy 1994) also place the low frequency to be about one tenth to one twentieth of the shedding frequency. Small undulations in the drag autocorrelation are due to oscillations in the drag coefficient at twice the shedding frequency. To illustrate the difference in shedding frequency between the high and low regimes, the autocorrelation of lift within each of these regimes was computed. From the dominant peak it was seen that the average shedding periods in regimes H and L are about 5.96 and 7.0, respectively. The corresponding mean shedding frequencies are 0.167 and 0.143, respectively. These frequencies computed from the autocorrelation are in good agreement with the average frequencies of 0.162 and 0.148 estimated in regimes H and L from figure 7(*c*). The corresponding average frequencies in the transition regimes I and D are 0.169 and 0.144. Thus there is about 20% variation in the shedding period over the low-frequency cycle see (figure 7*c*). A similar large variation in the shedding period over a low-frequency cycle has also been observed by Dauchy *et al*. (1997). The wide range of shedding frequency see in figure 7(*c*) is consistent with the range of frequency from 1.2 to 1.6 reported from experimental measurements (Fage & Johansen 1927; Abernathy 1962; Kiya & Arie 1980; Lisoski 1993).

3.4. *Streamwise velocity signature and its autocorrelation*

While global quantities such as drag and lift coefficients have clearly exhibited the presence of low-frequency unsteadiness, it is important to assess its impact on velocity measurements at isolated points in the wake. Such velocity measurements in the wake are more common than drag and lift measurements. Therefore, it remains to be seen if the low-frequency behaviour can be inferred from the single-point velocity signature. In figures 9(*a*), 9(*b*) and 9(*c*) temporal variations of the streamwise velocity component measured at three different downstream points $x = 1$, $x = 4$ and $x = 8$ are plotted. All three points are located at $y = 0.5$ and $z = \pi/2$. Oscillation in the streamwise velocity component at the shedding frequency is quite clear in the immediate wake ($x = 1$) and at $x = 8$, whereas at the intermediate location of $x = 4$ the streamwise velocity signature is far more complex. Occasional large departures from the near periodic behaviour can be seen as 'glitches', which are most evident at $x = 8$ for $t \approx 270$–285 and $t \approx 430$–460. As can be seen from figure 3(*b*), these time intervals precisely coincide with regime L. While the signature of the low-frequency unsteadiness is clearly evident at the downstream velocity probe at $x = 8$, this behaviour is not so evident in the other two near-wake velocity signatures.

The corresponding autocorrelations of the streamwise velocity component are shown in figures 9(*d*), 9(*e*) and 9(*f*). At $x = 8$ the most dominant peak in the autocorrelation corresponds to a shedding period of about 6.12 and the second most dominant peak corresponds to a low-frequency period of about 65.56. Both these values are in good agreement with those obtained from the drag and lift coefficients. The near-wake probe at $x = 1$ extracts a reasonably consistent shedding period of about 6.44 and a low-frequency period of about 65.48, even though the signature of the low frequency is not immediately apparent in the velocity signature. In spite of its

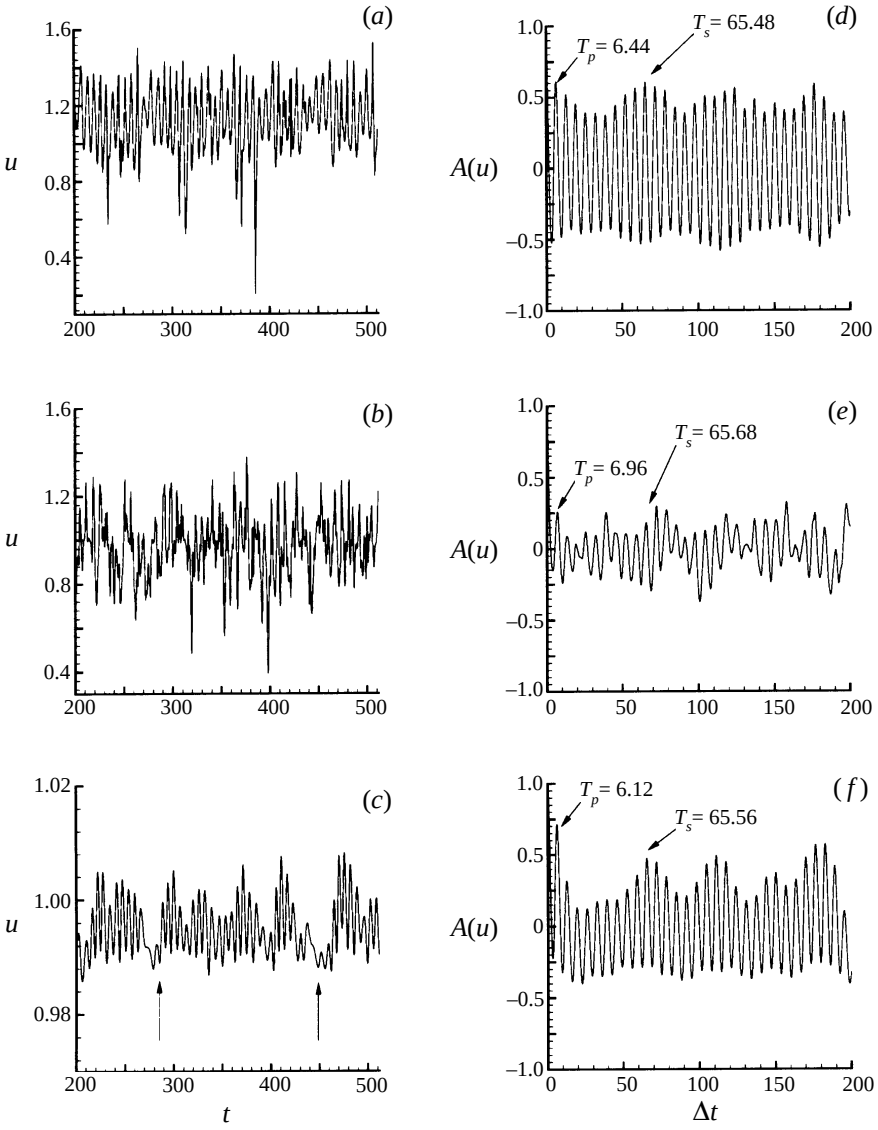

FIGURE 9. Time signals of the streamwise velocity component at three streamwise locations, (*a*) $x = 1$, (*b*) $x = 4$, and (*c*) $x = 8$. The cross-stream and spanwise locations of all three points are $y = 0.5$ and $z = \pi/2$, respectively. Note that the 'glitches' in (*c*) (marked with arrows) are qualitatively similar to those due to vortex dislocations, discussed in Williamson (1992). Corresponding autocorrelations of the velocity signals at (*d*) $x = 1$, (*e*) $x = 4$, (*f*) $x = 8$ are also shown. The periods of the primary Kármán shedding (T_p) and the secondary low-frequency unsteadiness (T_s) are marked. This clearly shows that the low-frequency unsteadiness is not just limited to global variables such as the lift and drag coefficients.

complexity, the velocity signature at $x = 4$ extracts a shedding period of about 6.96 and a longer period of about 65.68 can also be discerned. Hence, we believe that identification of the low-frequency unsteadiness, if any, is possible based solely on hot-wire probes, especially with the use of autocorrelation. Furthermore, the low-frequency unsteadiness is not just restricted to global measurements, it is a complex phenomenon experienced by the entire flow field. Based on their velocity and surface

pressure measurements Kiya & Sasaki (1985) also make a similar observation that the low-frequency unsteadiness is a global event felt everywhere within the recirculation bubble (and possible outside as well).

The 'glitches' in the streamwise velocity seen in figure 9(*c*) are similar to those observed by Williamson (1992) in the case of a circular cylinder at around a non-dimensional downstream distance of $x \approx 10$. He pointed out that these glitches are associated with vortex dislocations which appear in the wake transition regime. Velocity measurements at a series of downstream locations from $x = 5$ to $x = 40$ showed that, while the shedding frequency dominates the velocity signature at $x = 10$, the low-frequency unsteadiness associated with the glitches dominates the spectrum farther downstream. It was also observed that the shedding frequency with and without vortex dislocations is different and that the shedding frequency decreases with the presence of dislocations (also see Williamson 1996). The difference in the shedding frequency between the high- and low-drag regimes observed in the present simulation is consistent with these results.

3.5. *Pressure and Reynolds stress distributions in the wake*

The spatial distributions of the time- and span-averaged pressure coefficient within regimes H and L are presented in figures 10(*a*) and 10(*b*), respectively. Also marked in the figures as thick lines are the boundaries of the mean recirculation region. The non-dimensional length of the circulation region in the wake, defined as the distance from the base to the reattachment point (marked R in figure 10), is 1.70 and 3.13 in regimes H and L respectively. The corresponding half-heights of the recirculation region (defined as the maximum cross-stream distance from the centreline to the periphery of the mean recirculation region) in regimes H and L are 0.72 and 0.92. The repeated shrinkage and expansion of the mean recirculation region as the flow state changes between regimes H and L is consistent with previous observations of significant oscillation in the reattachment point along the longitudinal direction (Kiya & Sasaki 1985; Eaton & Johnston 1982). The non-dimensional length and half-height of the mean recirculation region computed over all the four regimes are 2.35 and 0.8, respectively. In comparison the experimental measurements of Bradbury & Moss (1975) and Leder (1991) at much higher Reynolds numbers of $Re = 2.64 \times 10^4$ and 2.8×10^4 showed a mean wake recirculation length of 1.92 and 2.50, respectively. The two-dimensional simulation predicts an extended mean recirculation region of length 13.75. Balachandar, Mittal & Najjar (1997) have summarized various experimental and computational results for the circular cylinder where the non-dimensional length of the mean recirculation region is observed to vary from 1.1 to 2.0. It is thus evident that the wake cavity length is significantly larger for the normal flat plate than for the circular cylinder.

The suction pressure in the wake is significantly higher in regime H than in regime L. For example the lowest pressure coefficient of about -3.0 is reached approximately at $x = 0.8$ in regime H, while the pressure coefficient in regime L reaches only about -1.6 at around $x = 1.5$. The significantly smaller mean wake bubble in region H is consistent with the higher suction pressure and the higher mean drag. The distributions of the time- and span-averaged pressure coefficient on the upstream and downstream faces of the normal flat plate computed separately in regimes H and L are also shown in figure 6. Regime L yields a near constant pressure coefficient value of -1.35 on the downstream face while Regime H results in a higher suction pressure coefficient of -2.1. The overall flow pattern falls between those of regimes H and L, leading to a base pressure coefficient of -1.63. In comparison, the two-dimensional computation

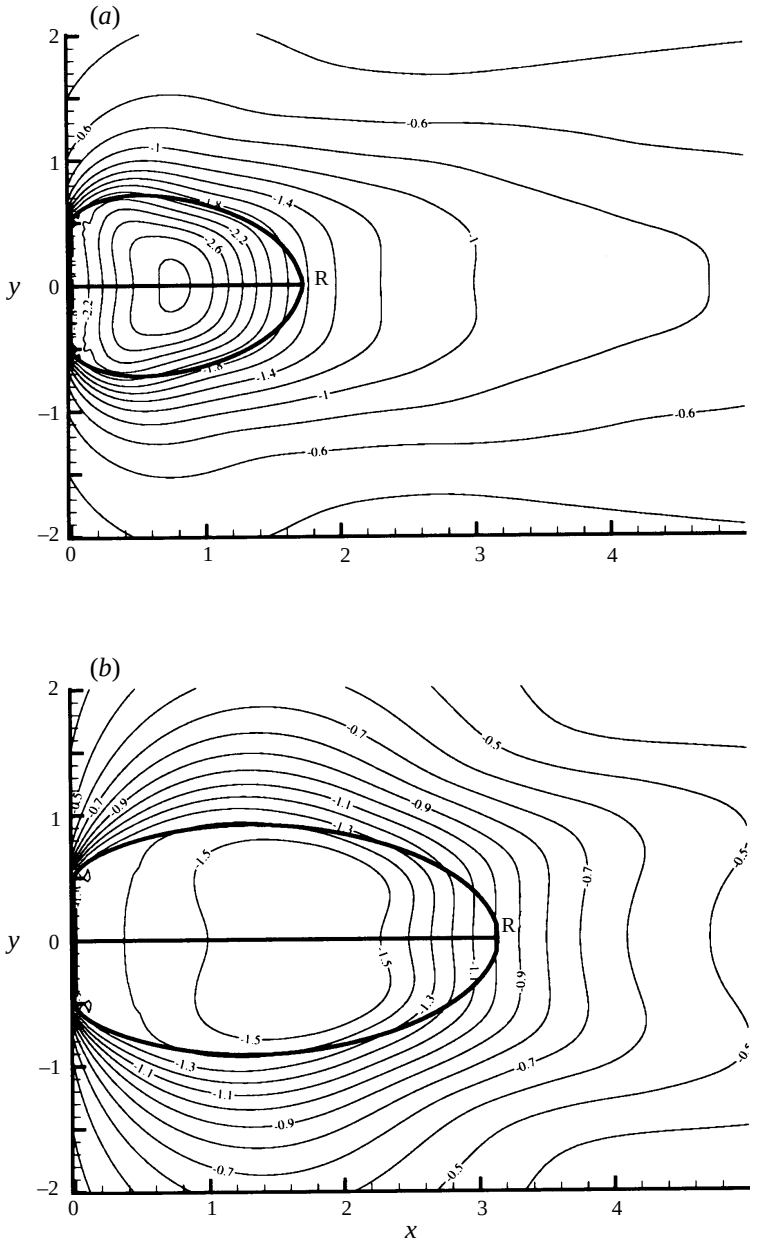

FIGURE 10. Contour plots of time- and span-averaged pressure coefficient in (*a*) regime H and (*b*) regime L. The contour levels in (*a*) extend from -3.0 to -0.4 in steps of 0.1 and in (*b*) from -1.5 to -0.4 in steps of 0.1. The value of the base pressure coefficients on the downstream face of the normal plate are -2.1 and -1.5 in regimes H and L, respectively. The mean wake recirculation region for each regime is identified by the zero-streamline of the time- and span-averaged velocity field and drawn as thick contour lines. The reattachment point is marked R. The length of the mean wake recirculation region is computed from $x = 0$ to R and the half-height is defined as the maximum cross-stream (y) distance from the centreline to the periphery of the mean recirculation region.

predicts a base pressure coefficient of -2.8. Thus the behaviour of regime H is closer to the two-dimensional simulation than regime L.

Consistent with the smaller compact recirculation region, in regime H the Reynolds stresses are distributed in the wake close to the base of the normal plate, whereas in regime L the Reynolds stresses are distributed farther away from the immediate base and in fact both the streamwise normal and shear stresses are nearly zero for $x < 0.75$. Furthermore, the peak Reynolds stresses in regime H are nearly 60% stronger than those in regime L (Najjar & Balachandar 1997). The low level of Reynolds stresses in the near-wake region for regime L suggests that here the shear layers are nearly two-dimensional and reasonably time independent and therefore the delayed roll-up process contributes to the Reynolds stresses only away from the immediate wake of the normal plate. These differences in the Reynolds stress distribution are similar to those observed between two-dimensional and three-dimensional simulations by Mittal & Balachandar (1995*a*) for a circular cylinder. The higher suction pressure and the significantly enhanced drag in regime H are directly related to the stronger Reynolds stresses observed in the immediate wake. A significant contribution to the Reynolds stresses come from the dynamics of the Kármán vortices. Therefore the fundamental difference in the Kármán vortex dynamics between regimes H and L will be explored below in the following section.

4. Kármán vortex dynamics

4.1. *Phase average and swirling strength*

In order to clearly identify the spanwise Kármán and streamwise vortices and gain further insight into their dynamics, in this section we will first define the vortex identification technique employed here along with the necessary phase-averaging technique. The spanwise and streamwise vortices are visualized by plotting contours of their *swirling strength*, λ_i, defined as the imaginary part of the complex eigenvalue of the velocity-gradient tensor, $\boldsymbol{\nabla u}$. In regions dominated by local straining motion all three eigenvalues of the velocity gradient tensor are real, whereas when vortical motion locally dominates over the straining motion, two of the eigenvalues of $\boldsymbol{\nabla u}$ becomes complex-conjugate (Perry & Chong 1987). In this case it can be shown that there exists a plane where local streamlines are spiralling, suggesting the presence of a vortex (Chong, Perry & Cantwell 1990; Zhou *et al.* 1997). Furthermore, the magnitude of the imaginary part of the complex-conjugate eigenvalues captures the strength of the spiralling motion and is thus termed the swirling strength, and the corresponding eigenvectors define the plane of spiralling motion (Zhou *et al.* 1997). At spatial locations where all three eigenvalues are real, λ_i is set to zero; thus regions of positive λ_i can be used to identify vortices with the magnitude of λ_i representing the local vortex strength (Dallmann *et al.* 1991; Mittal & Balachandar 1995*b*; Zhou *et al.* 1997). The swirling strength has the same dimension as vorticity (or velocity gradient); in a purely vortical flow (without any strain) its magnitude is half of the local vorticity. The swirling strength has the advantage that it avoids misinterpreting shear layers from rolled-up vortices. This vortex identification procedure is applied here to the full-three-dimensional flow field and the corresponding three-dimensional swirling strength, denoted by $\lambda_{i,3D}$, simultaneously extracts both the spanwise and streamwise vortices.

To individually extract the spanwise and streamwise vortices we also employ the vortex identification procedure to velocity data on two-dimensional (x, y)-, (y, z)- and (x, z)-planes (Zhang, Balachandar & Tafti 1997). The corresponding planar swirling strengths will be denoted by $\lambda_{i,xy}$, $\lambda_{i,yz}$ and $\lambda_{i,xz}$, respectively. The structure of spanwise

Kármán vortices is extracted from the (x, y)-swirling strength, $\lambda_{i,xy}$, and will be denoted as $\lambda_{i,p}$ (to indicate primary vortex structure). This quantity is in general three-dimensional (dependent on x, y and z) due to distortions in the spanwise Kármán vortices along the spanwise (z) direction. The streamwise vortices, also often referred to in the literature as the streamwise ribs, that connect the adjacent spanwise Kármán vortices are normally tilted in the (x, y)-plane and are not purely oriented along the streamwise (x) direction. A combined measure of (y, z) and (x, z) swirling strengths as given by $\lambda_{i,s} = (\lambda_{i,yz}^2 + \lambda_{i,xz}^2)^{1/2}$ will be used to identify these vortices. Here, we will correctly refer to $\lambda_{i,s}$ as the cross-span swirling strength or the secondary swirling strength (hence the subscript s), whereas, for conformity, the cross-span vortices will be addressed by their commonly used terminology as the streamwise vortices or streamwise ribs.

In order to reduce the background fluctuations and enhance the Kármán vortex dynamics, here we follow the phase-averaging technique originally proposed by Reynolds & Hussain (1972) and Cantwell & Coles (1983) and apply it separately within the different regimes. The flow variables such as $(\boldsymbol{u}, p, \lambda)$ are considered to consist of three main components: a time- and span-averaged mean $(\bar{\boldsymbol{u}}, \bar{p}, \bar{\lambda})$, a periodic $(\tilde{\boldsymbol{u}}, \tilde{p}, \tilde{\lambda})$, and a random component $(\hat{\boldsymbol{u}}, \hat{p}, \hat{\lambda})$ as follows: $(\boldsymbol{u}, p, \lambda) = (\bar{\boldsymbol{u}}, \bar{p}, \bar{\lambda}) + (\tilde{\boldsymbol{u}}, \tilde{p}, \tilde{\lambda}) + (\hat{\boldsymbol{u}}, \hat{p}, \hat{\lambda})$. According to this definition the periodic component, which arises from the dominant shedding process, and the random component together contribute to the total perturbation away from the time- and span-average (i.e. $(\boldsymbol{u}', p', \lambda') = (\tilde{\boldsymbol{u}}, \tilde{p}, \tilde{\lambda}) + (\hat{\boldsymbol{u}}, \hat{p}, \hat{\lambda})$). The coherent component, also referred to as the phase-averaged component, denoted by $(\bar{\tilde{\boldsymbol{u}}}, \bar{\tilde{p}}, \bar{\tilde{\lambda}})$, is defined as the sum of the time- and span-averaged and periodic parts as: $(\bar{\tilde{\boldsymbol{u}}}, \bar{\tilde{p}}, \bar{\tilde{\lambda}}) = (\bar{\boldsymbol{u}}, \bar{p}, \bar{\lambda}) + (\tilde{\boldsymbol{u}}, \tilde{p}, \tilde{\lambda})$.

In the present study, each shedding cycle, which is arbitrarily defined to start with a local peak in the lift coefficient and extend up to the next peak, is divided into eight phases of equal extent each covering one-eighth of the shedding cycle. All the three-dimensional data dumps are first sorted according to the four flow regimes: H, L, D and I, respectively. Within each regime the dumps are further sorted into the eight phase bins, according to the time of the data dump (or the phase) within the shedding cycle. All data sets in a phase bin within each regime, are averaged to obtain the phase-averaged or the coherent component. The phase-averaging procedure also includes an average along the span and therefore the phase-averaged variables are two-dimensional and will be denoted by $[\bar{\tilde{\boldsymbol{u}}}]_k(x, y)$ or $[\bar{\tilde{\lambda}}]_k(x, y)$, where $k = 1, \ldots, 8$ is the phase bin number. The large number of data sets considered in this study along with the limited number of phase bins guarantee a reasonably converged phase average within each bin.

4.2. *Phase-averaged spanwise swirling strength*

First, the evolution of the spanwise Kármán vortices are followed separately in regimes H and L. Attention is focused on phase-averaged coherent component of the spanwise swirling strength, $[\bar{\tilde{\lambda}}_{i,p}]_k$. Figure 11 (*a–d*) presents contours of $[\bar{\tilde{\lambda}}_{i,p}]_k$ for the first four phases ($k = 1$–4) in regime H. This sequence covers one half of the shedding cycle, and swirling strength for phases 5–8 can be obtained from the other four phases with appropriate symmetry about the wake centreline of the following form: $[\bar{\tilde{\lambda}}_{i,p}]_k(x, y) = [\bar{\tilde{\lambda}}_{i,p}]_{k-4}(x, -y)$. Hence, the evolution of the Kármán vortices over the entire shedding cycle can be followed. From figure 11 the separated shear layers are seen to roll up and form new spanwise vortices very close to the flat plate within the region of $x < 1$. The separation of the rolled-up vortices from the shear layers seems to be complete within two plate heights downstream of the normal plate ($x < 2$). The coherence of the Kármán vortices is maintained up to $x = 10$ and beyond. The corresponding four

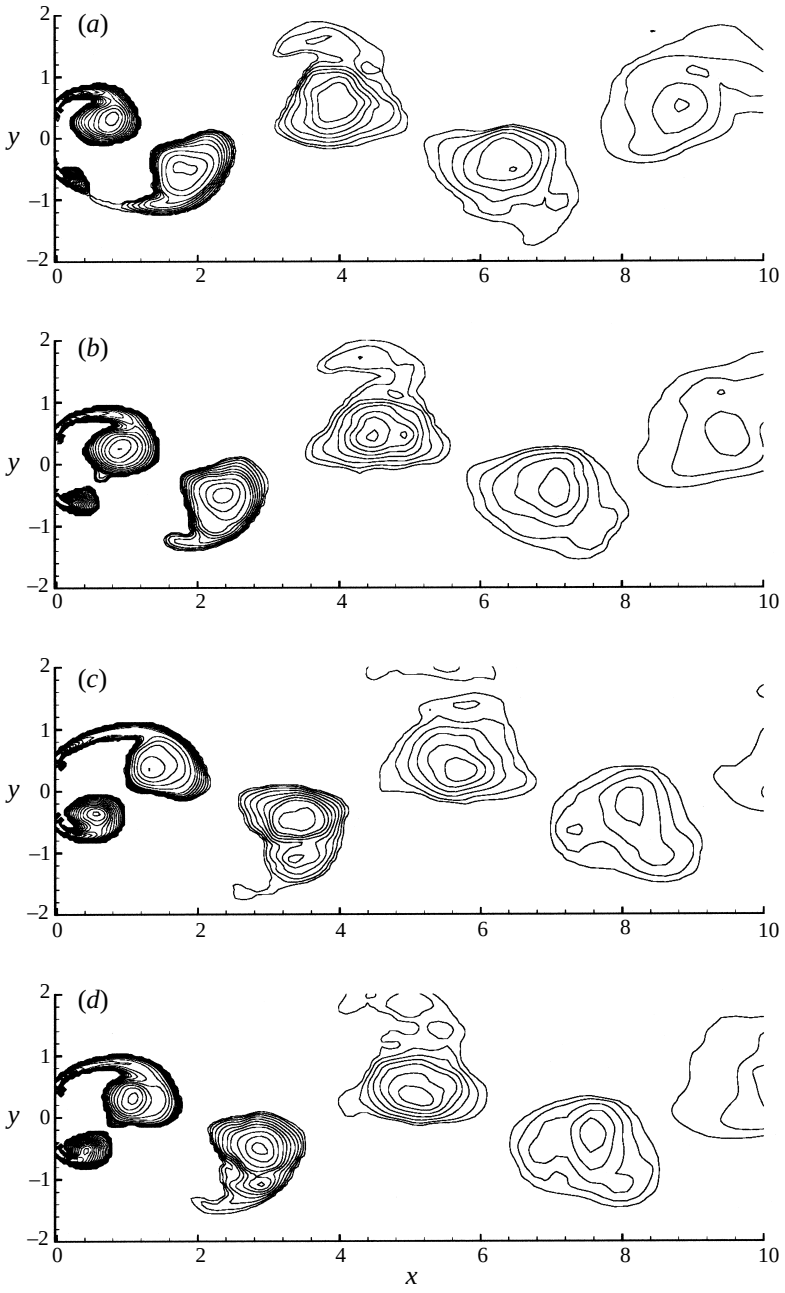

FIGURE 11. Contours plots of the phase-averaged coherent spanwise swirling strength, $[\tilde{\bar{\lambda}}_{i,p}]_k$ in regime H: (*a*) phase 1, (*b*) phase 2, (*c*) phase 3 and (*d*) phase 4. Phases 5–8 can be obtained from the above four by reflectional symmetry about the wake centreline. Flow is from left to right with the normal plate at $x = 0$ extending from $-0.5 < y < 0.5$. Contour levels are: from 0.125 to 1.0 in steps of 0.125 and from 1.0 to 5.0 in steps of 0.25.

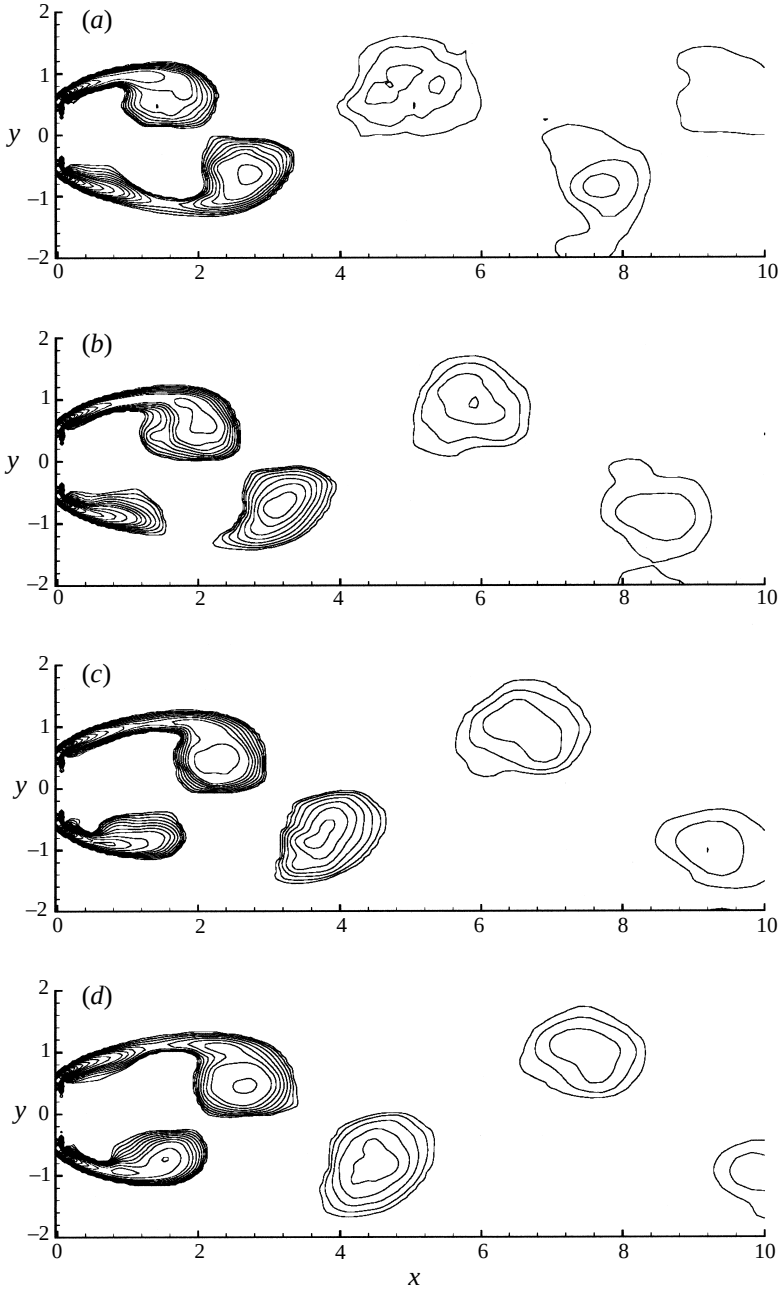

FIGURE 12. Same as figure 11 but for regime L.

phases in regime L are plotted in figure 12(*a–d*). Significant differences in the wake dynamics can be observed between regimes H and L. In regime L the roll-up of the separated shear layers appears to be complete only farther downstream for $x > 2$ and correspondingly the vortex pinch-off from the shear layer is delayed to $x \approx 3$. This difference in the dynamics of the spanwise vortices clearly explains the shrinkage of the mean recirculation region from regime L to H.

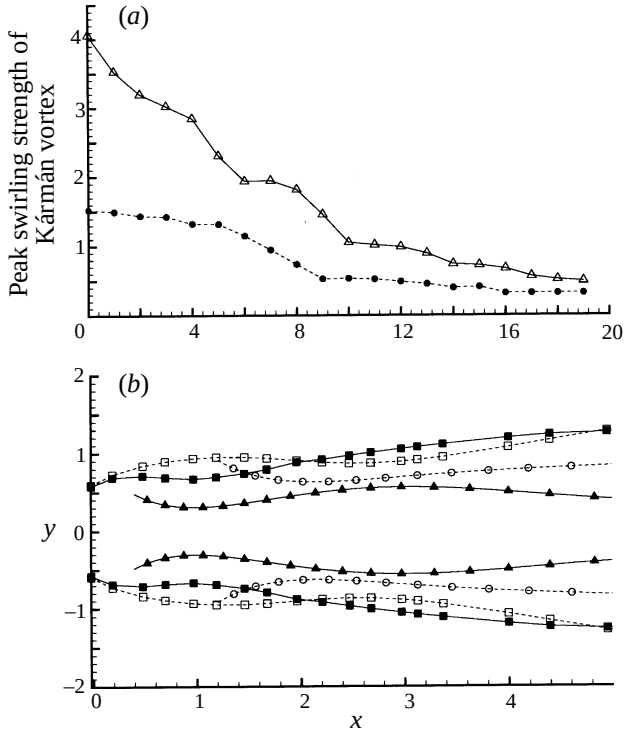

FIGURE 13. (*a*) Streamwise evolution of the peak strength of the coherent Kármán vortex core in regime H (—— △ ——) and regime L (– – – ● – – –). The peak strength of the vortex core is defined as the maximum magnitude of the spanwise swirling strength within the vortex (see figures 11 and 12). (*b*) Typical Kármán vortex trajectories (circles and triangles) and the location of the upper and lower shear layer centres, y_c (squares), in regimes H and L. Open and closed symbols denote regimes L and H, respectively.

Figure 13(*a*) presents the evolution of the coherent vortex core strength as it travels in the downstream direction for regimes H and L, measured in terms of the maximum magnitude of $\tilde{\lambda}_{i,p}$ within the vortex core. Since vorticity is approximately twice the swirling strength, the peak vorticity magnitudes in regimes H and L are approximately 8 and 3, respectively. Near the separation point ($x \sim 0$) the initial strength of the Kármán vortex in regime H is a factor of 2.5 higher than that in regime L. Although the spanwise vortices in regime H decay at a faster rate as they evolve downstream and appear to approach the strength of the corresponding vortices in regime L, even at $x > 15$ the spanwise Kármán vortices in regime H are nearly twice as strong as those in regime L. It must be stated in passing that the magnitude of phase-averaged $\lambda_{i,p}$ decays to about 25% to 30% of its initial value by around $x = 10$ to 15 in both regimes H and L. This compares favourably with the experimentally measured fraction of initial circulation in the convected vortices in the region $x = 10$ to 16 (60% by Fage & Johansen 1927, 43% by Roshko 1954, 30% by Bloor & Gerrard 1966 and 26% by Davies 1976).

The trajectories of the clockwise and counter-clockwise Kármán vortex cores in the upper and lower halves of the (x, y)-plane are plotted in figure 13(*b*) for regimes H and L. In both regimes the spanwise vortices evolve nearly parallel to the x-axis. The primary differences are that in regime H the vortices form closer to the plate and that

they remain closer to the wake centreline. Also plotted in this figure are the centres of the time-averaged upper and lower shear layers, y_c, for both regimes H and L. Following the conventional definition used in mixing layers, y_c is defined as the transverse location at which the time- and span-averaged streamwise velocity has a value of $0.67\Delta\bar{u}+\bar{u}_{min}$, where $\Delta\bar{u} = \bar{u}_{max}-\bar{u}_{min}$ is the velocity difference between the maximum velocity, $\bar{u}_{max}$, on the high-speed side and the minimum velocity, $\bar{u}_{min}$, on the low-speed side. The position of the mean shear layers as well as the Kármán vortex trajectories suggest that as the wake goes through the low-frequency cycle, the shear layers will appear to undergo a transverse oscillation. Eaton & Johnson (1982) have conjectured such a low-frequency vertical oscillation of the shear layer. Experimental measurements by Kiya & Sasaki (1985) have confirmed the vertical oscillation of the shear layer but the amplitude of oscillation was observed to be only 2.5% of the blunt flat plate's thickness. Recent measurements in the shear layers of a circular cylinder (Prasad & Williamson 1997) have shown that the vertical motion of the shear layer is at most 8% of the shear layer thickness, which itself is a small fraction of the cylinder diameter.

Interpretation of the shear layer centre shown in figure 13(*b*) requires some caution. First of all, y_c is obtained from a mathematical definition based on the time-averaged flow, so one is able to obtain a value for y_c even downstream after the shear layers have rolled up into Kármán vortices. Although the difference in centres of the shear layers between regimes H and L at $x = 1$ appears to be about 0.2, the roll-up of the shear layers in regime H occurs close to the plate, well upstream of $x = 1$. For $x < 0.5$, the shear layer centres in regimes H and L are less than 10% of the plate height apart. This is still substantially larger than the vertical movement estimated by Prasad & Williamson (1997), which may be the result of differences in the geometry and the Reynolds number. Nevertheless, characterization of the low-frequency unsteadiness as 'shear layer flapping' (as sometimes done in the past) does not provide a complete description of the observed behaviour. The forward and backward movement of the formation region is much more pronounced than the up and down motion of the shear layers. Of course these two movements are interrelated. Furthermore, as will be seen below, the low-frequency unsteadiness has its origin in the three-dimensional state of the wake. Therefore here we will consistently adhere to the terminology 'low-frequency unsteadiness'.

4.3. *Connection to drag and lift variation*

The above observations on the dynamics of the spanwise Kármán vortices in regimes H and L are completely consistent with the drag and lift variations reported in the earlier sections. First of all, the spanwise vortices in regime H are compact and they form close to the base of the normal plate and their dynamics is such that the resulting time- and span-averaged mean wake recirculation region is small and compact (see figure 10*a*). On the other hand, the roll-up process is delayed in regime L resulting in an extended mean wake recirculation region. The periodic shedding of the strong compact spanwise vortices in regime H directly contributes to the enhanced Reynolds stress components in the immediate wake. On the other hand, in regime L the Reynolds stresses are weaker and are distributed farther away from the base, consistent with the observed delayed vortex roll-up process. As a result of the enhanced Reynolds stresses in the immediate wake, the associated time- and span-averaged mean pressure along the base is significantly lower in regime H than in regime L (Mittal & Balachandar 1995*a*), contributing to significantly higher drag in regime H when compared to regime L. The periodic exchange between the shedding of strong compact Kármán vortices of regime H and weaker shedding process in regime L directly contributes towards the

observed low-frequency component of the drag coefficient. Owing to the symmetry of the wake about its centreline, the mean lift within each shedding cycle is constrained to be nearly zero. Thus there is no low-frequency component superposed on the lift coefficient, as in the drag coefficient.

For the normal plate, the fluctuating lift force over each shedding cycle is due to the fluctuating viscous shear stress on the back side of the plate. The periodic shedding of strong compact clockwise and counter-clockwise Kármán vortices in regime H directly translates to a large-amplitude fluctuation in the lift coefficient over each shedding cycle, whereas in regime L the less compact Kármán vortices shed farther away from the base have less of an impact on the viscous shear stress that acts on the back face of the normal flat plate. As a result, the variation in lift coefficient during the shedding process is weak in regime L. On the other hand, fluctuations in the drag force are due to oscillations in the pressure distribution around the normal plate, primarily at twice the shedding frequency. The strong compact vortices of regime H correspond to large pressure fluctuations as well. As indicated in Mittal & Balachandar (1995*a*), although pressure fluctuates at the shedding frequency, its distribution around the normal plate at this frequency has a near front–back symmetry that it makes little contribution to drag. On the other hand, fluctuation in pressure at twice the shedding frequency is also strong. At this frequency, the pressure distribution around the normal plate is such that it makes a strong contribution to drag variation. Owing to the weaker vortex shedding process in regime L, $\tilde{u}$ and $\tilde{v}$ are generally smaller in magnitude and distributed farther away from the base. Based on this, the near absence of drag variation during a shedding cycle in regime L can be justified.

Finally, there is ample evidence to suggest an inverse relation between the strength and coherence of the shed spanwise Kármán vortices and the period at which they are shed. This also translates to an inverse relation between the length of the Kármán vortex formation region (or the length of the mean wake recirculation region) and the frequency of shedding. For example, an increase in net circulation of the shed vortices with increasing Reynolds number contributes to an increase in the shedding frequency. The shedding process can be considered to be the act of a newly forming spanwise vortex moving towards the centreline and cutting off the continued supply of vorticity to the earlier vortex of opposite sign from its shear layer. The movement of these vortices is in turn governed by their mutual induction. Thus with increasing strength of the spanwise vortices, their induced velocities increase, resulting in reduced shedding period and increased shedding frequency. This line of argument sufficiently explains the observed low-frequency modulation of the shedding frequency.

Two distinct states of vortex shedding have also been observed by Kiya & Arie (1980) in their discrete-vortex simulations of flow over a normal plate. Regimes L and H closely resemble their state I and state II vortex shedding. They observe that in stage I, the separated shear layers extend farther downstream and result in a formation region of length 55% more than in state II. While in the present computation a continuous low-frequency switching between regimes H and L is observed, in the discrete-vortex simulations of Kiya & Arie (1980) state I (or regime L) was observed only during the initial transients of the computation. State I was generally observed to be unstable and give way to an eventual state II (or regime H) behaviour. As we will see below, this may be an artifact of the two-dimensional limitation of their discrete-vortex simulation. Nevertheless, many of the features of regimes H and L outlined above are in agreement with the observations of Kiya & Arie (1980). They observe the non-dimensional shedding frequency to be approximately 0.25 in state II and 0.2 in state I. As pointed out by Kiya & Arie (1980), these values are somewhat larger, owing

to the two-dimensional nature of the discrete-vortex simulations, and do not quantitatively compare with the shedding frequencies of 0.162 and 014 for regimes H and L. But the qualitative trend remains the same in both simulations. Their time-averaged C_D measured in state I was approximately 2.0, while state II yielded a much higher mean drag coefficient of about 3.0. Furthermore, consistent with the present observations, it can be seen in their time history of C_D that the drag variation over a shedding cycle in state I was negligible when compared to the strong cyclic variation in state II.

An interesting comparison can also be made with the behaviour of wakes behind cylinders undergoing forced vibration. In the lock-in (or synchronized) regime, the formation length decreases systematically with increased amplitude of vibration of the cylinder (Griffin & Votaw 1972 and Griffin & Ramberg 1974). While the formation length is intimately related to the streamwise length of the mean recirculation region, the amplitude of vibration of the cylinder in the forced case plays an analogous role to the amplitude of drag and lift variation in the unforced wake. Furthermore, Griffin and coworkers observed that as the frequency of forcing is increased the scale of the formation region decreases. Thus the relation between the amplitude, frequency and the nature of the vortex roll-up process observed in the present computation in regimes H and L appears to hold good even in the case of forced wakes.

5. Distinct modes of three-dimensionality

The above section clearly characterized the two different states of Kármán vortex shedding in regimes H and L. In this section we will explore mechanisms responsible for these two distinct states of vortex shedding. The marked difference between the two-dimensional and three-dimensional simulation results, along with the absence of a strong low-frequency component in the case of the two-dimensional simulation, suggests that the difference between regimes H and L has its root in their respective three-dimensional structure. Figure 14(*a*) shows a perspective view of the three-dimensional vortical structure in regime H, plotted in terms of an iso-surface of three-dimensional swirling strength, $\lambda_{i,3D} = 1.0$. The flow is from left to right and the corresponding top and bottom views are shown in figures 14(*b*) and 14(*c*). This instantaneous plot at $t = 416$ corresponds to an instance in regime H. Marked in this figure are two generations of clockwise Kármán vortices (CR0 and CR1) appearing from the top shear layer and three generations of counterclockwise vortices (CCR0, CCR1 and CCR2) appearing from the bottom shear layer. Noticeable spanwise distortion is present even in the newly forming counterclockwise-rotating Kármán vortex (CCR0), which is clearly visible in the bottom view. The distorted spanwise vortices are connected by streamwise vortices (or streamwise ribs). The spanwise extent of the computational domain is sufficiently wide to accommodate about five pairs of streamwise vortices in the near-wake region (see §6 for details).

The organization of spanwise and streamwise vortices in figure 14, although hardly perfect, is reasonably well structured, especially when compared to the corresponding three-dimensional structure in regime L. In figures 15(*a*), 15(*b*) and 15(*c*), the perspective, top and bottom views of an iso-surface of $\lambda_{i,3D} = 1.0$ are shown at $t = 456$ in regime L. This time instant corresponds to a point of minimum lift during regime L. The delayed roll-up of the spanwise Kármán vortices is evident. The counter-clockwise-rotating spanwise vortex (CCR1) that has just detached from the bottom shear layer is seen to be torn apart in the spanwise direction. The detached clockwise vortex CR1 is in fact distorted to an extent that it cannot be clearly identified. Many

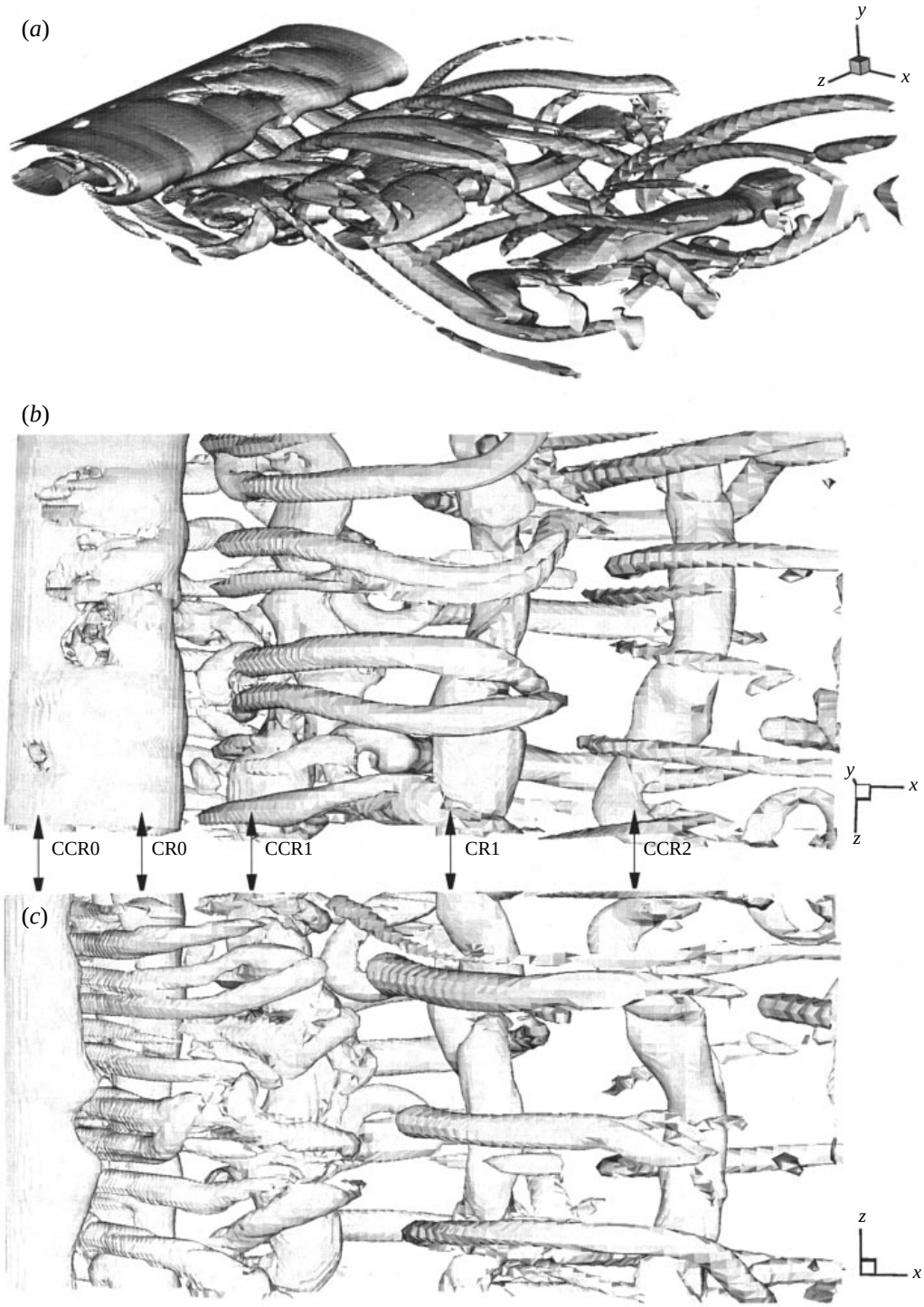

FIGURE 14. Iso-surface of the three-dimensional instantaneous swirling strength, $\lambda_{i,3D} = 1.0$, at $t = 416$, in regime H. (*a*) Perspective, (*b*) top, and (*c*) bottom views of the iso-surface. Flow is from left to right. Clockwise-rotating (CR) and counterclockwise-rotating (CCR) Kármán vortices are marked with arrows.

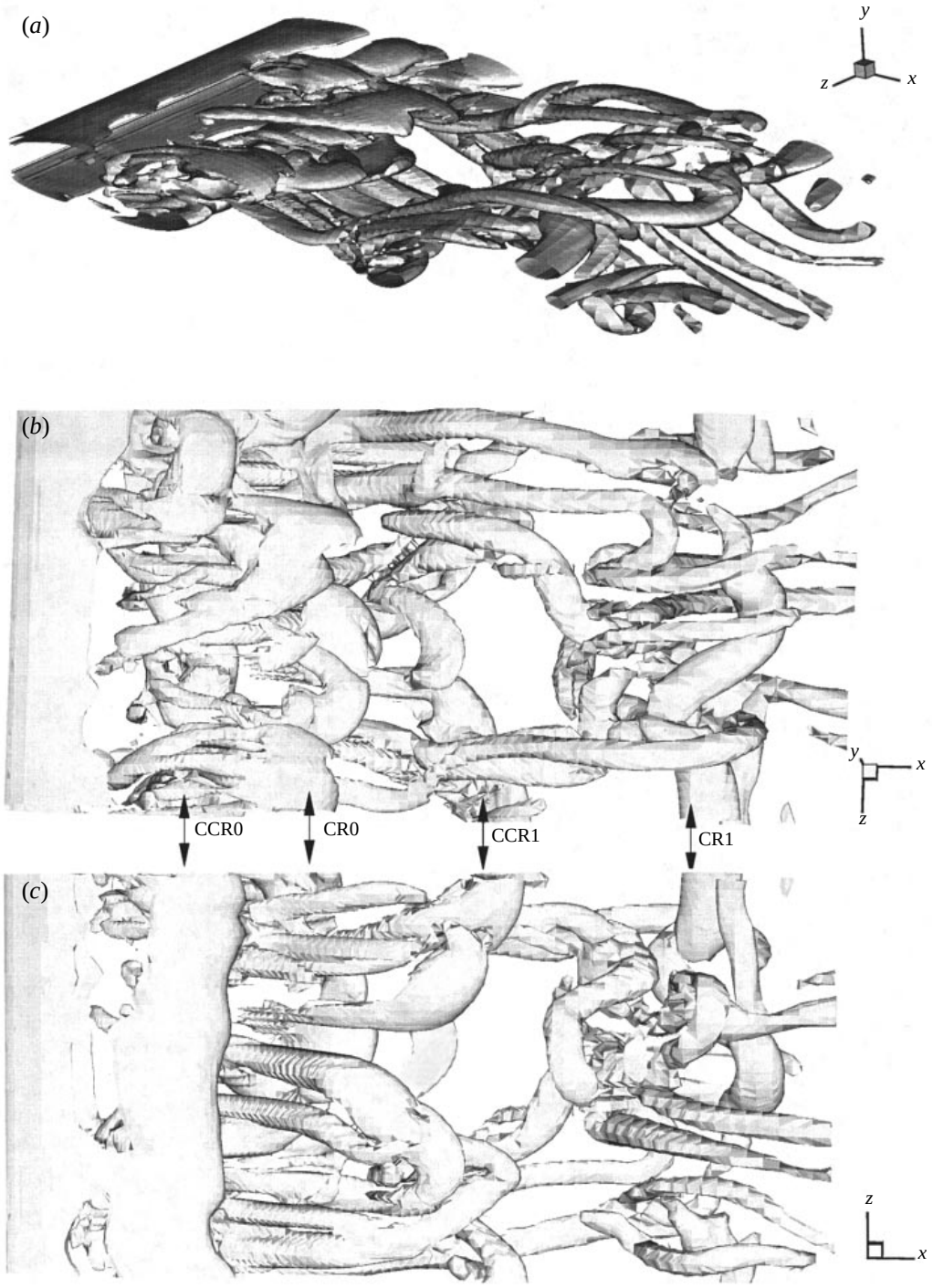

FIGURE 15. Same as figure 15 but at $t = 456$, in regime L.

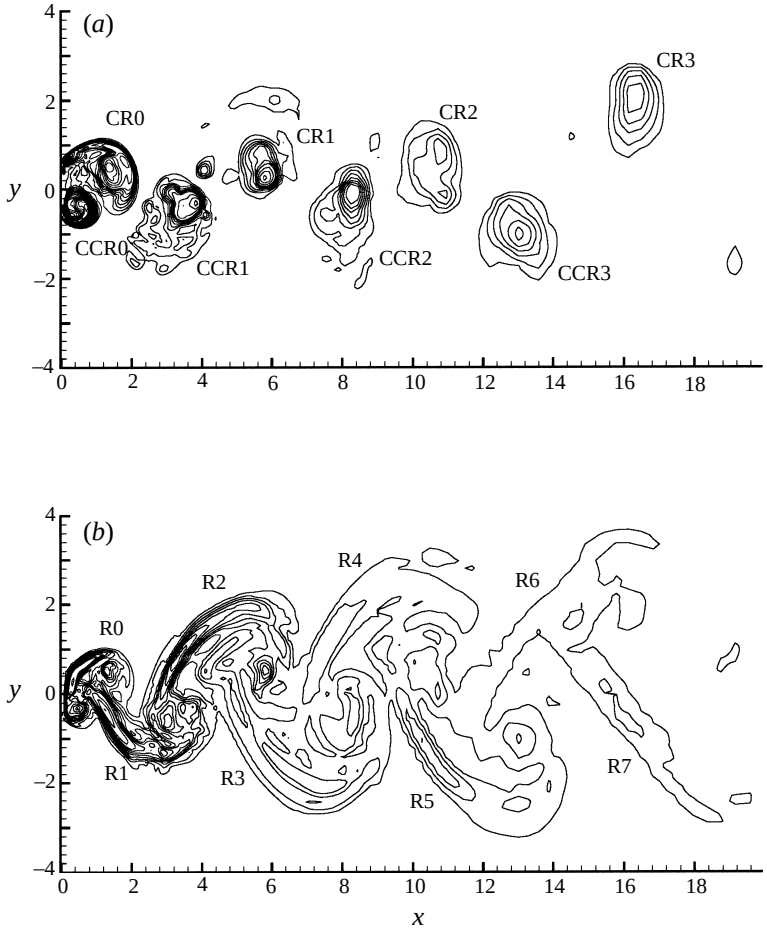

FIGURE 16 (a, b). For caption see facing page.

streamwise vortices can be identified but their size, shape and spatial organization are far more irregular. Some of the streamwise looking vortices appear to have their origin in the pieces of distorted spanwise vortices that are torn apart and tilted in the streamwise direction. The conversion of spanwise vorticity from the Kármán vortex cores into streamwise vortices is at the heart of core and elliptic instability (Pierrehumbert & Widnall 1982; Corcos & Lin 1984; Waleffe 1990) and mode-A instability of bluff body wakes (Williamson 1996). A similar scenario of large chunks of spanwise vorticity escaping from the core of Kármán vortices to form streamwise vortices has previously been identified in the context of spanwise subharmonic instability and period doubling in the wake of a circular cylinder (Mittal & Balachandar 1995*b*).

Apart from the above two time instants, the three-dimensional vortex structure behind the normal plate was carefully analysed at several other times as well. In addition to the three-dimensional visualization, the distribution of swirling strength (or vorticity) was examined systematically on a series of (x, y)- and (y, z)-planes, at the various time instants considered. The detailed structure of both the spanwise and streamwise vortices showed variability from shedding cycle to shedding cycle in both regimes H and L. Nevertheless, the following common features can be identified to be

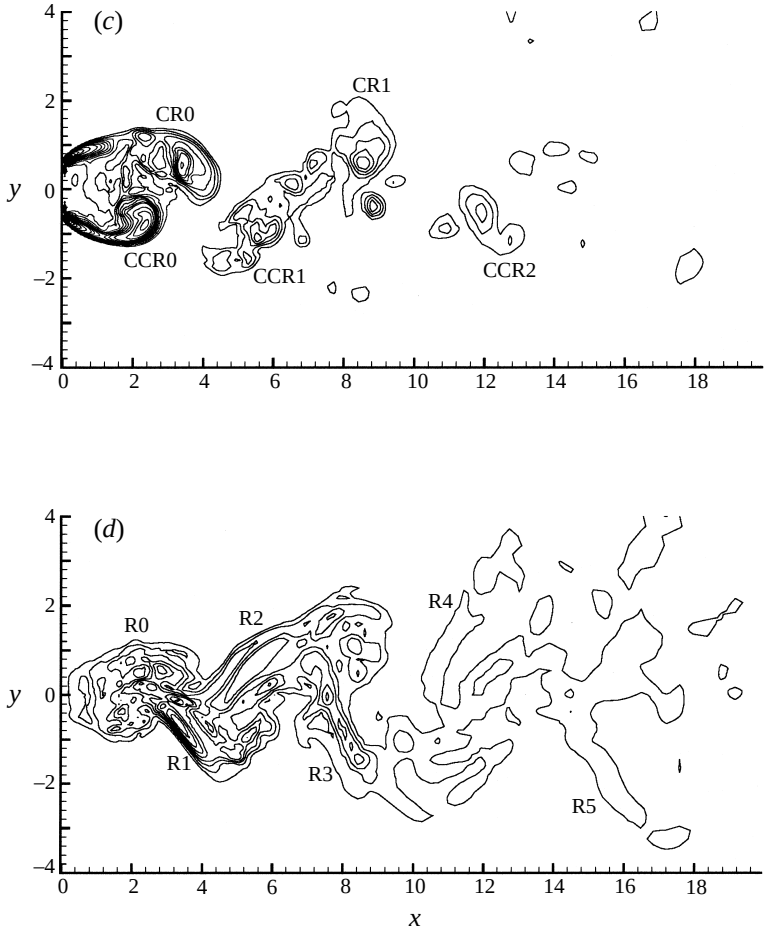

FIGURE 16. (*a*, *c*) Contour plots of span-averaged instantaneous spanwise swirling strength, $\langle \lambda_{ci,p} \rangle_z$, in (*a*) regime H at $t = 416$ and (*c*) regime L at $t = 456$. Clockwise-rotating (CR) and counterclockwise-rotating (CCR) Kármán vortices are numbered and marked. (*b*, *d*) Contour plots of span-averaged instantaneous streamwise swirling strength $\langle \lambda_{ci,s} \rangle_z$, in (*b*) regime H at $t = 416$ and (*d*) regime L at $t = 456$. Streamwise ribs connecting the Kármán vortices are marked as R0, R1, etc. Contour levels are 0.125 to 1.0 in steps of 0.125 and from 1.0 to 5.0 in steps of 0.25.

characteristic of regimes H and L. In regime H the Kármán vortices undergo significant distortion in the spanwise direction, but generally remain distinct from the streamwise vortices. In each braid region between the Kármán vortices, a finite number of streamwise vortices are seen, which remain coherent, concentrated and spatially compact. On the other hand, in regime L the spanwise vortices are torn apart and broad regions of streamwise vorticity can be identified. Although some compact streamwise vortices can be identified, the distribution of streamwise vorticity is in general diffused and not organized. In what follows the above observations will be quantified with appropriate statistics.

5.1. *Span-averaged statistics*

The three-dimensional vortical structures shown in figures 14 and 15 clearly include both the spanwise Kármán vortices and the streamwise vortical ribs. To separately quantify the spanwise and streamwise vortices, the instantaneous velocity field was

used to compute the corresponding spanwise and cross-span swirling strengths, $\lambda_{i,p}$ and $\lambda_{i,s}$. The span-averaged values of these two quantities is defined as

$$\langle\lambda_{i,p}\rangle_z = \frac{1}{L_z}\int_0^{L_z}\lambda_{i,p}\,\mathrm{d}z \quad \text{and} \quad \langle\lambda_{i,s}\rangle_z = \frac{1}{L_z}\int_0^{L_z}\lambda_{i,s}\,\mathrm{d}z. \tag{2}$$

Thus, contours plots of $\langle\lambda_{i,p}\rangle_z$ and $\langle\lambda_{i,s}\rangle_z$ on the (x,y)-plane are expected to provide information on the span-averaged strength of spanwise Kármán and streamwise rib vortices, respectively. Figures 16(*a*) and 16(*b*) show contour plots of $\langle\lambda_{i,p}\rangle_z$ and $\langle\lambda_{i,s}\rangle_z$ in regime H corresponding to the time instant shown in figure 14. As can be seen in figure 16(*a*), $\langle\lambda_{i,p}\rangle_z$ clearly extracts Kármán vortices that are typical of regime H, and they are marked CR0, CCR0, CR1, CCR1, etc. In figure 16(*b*), the streamwise ribs connecting the spanwise vortices can be identified and they are marked R0, R1, etc. However, the spanwise Kármán vortices can also be identified in figure 16(*b*). This is due to the strong bending and distortion of the spanwise Kármán vortices and as a result they make a significant contribution to the cross-span swirling strength as well. In other words, $\langle\lambda_{i,s}\rangle_z$ receives contributions both from the streamwise vortices and the distorted spanwise Kármán vortices. Thus the unconditional spanwise average of cross-span swirling strength is not entirely successful in isolating the streamwise vortical ribs.

The corresponding span-averaged measures of spanwise and cross-span swirling strength corresponding to figure 15 of regime L are shown in figures 16(*c*) and 16(*d*). To facilitate direct comparison, the contour levels are maintained the same in all the four plots. Consistent with the tearing of the spanwise vortices, in figure 16(*c*) coherent spanwise vortices are not observed downstream of $x = 12$. As pointed out earlier, the plot of $\langle\lambda_{i,s}\rangle_z$ in figure 16(*d*) receives contributions both from the streamwise rib vortices and the distorted spanwise Kármán vortices. Nevertheless, in comparison to figure 16(*b*), this plot suggests spatially distributed streamwise vorticity with only a weak resemblance to streamwise vortical ribs connecting spanwise vortices. Based on these figures it is tempting to conclude that the streamwise vortex ribs are more active in regime H than in regime L. Such a conclusion is not supported by the three-dimensional visualizations (figures 14 and 15), since significant streamwise rib activity is seen in both regimes H and L. The proper interpretation of figures 16(*b*) and 16(*d*) is that in regime H, the streamwise vortices are coherent along the spanwise direction in order to make a significant contribution to the spanwise average, whereas in regime L the streamwise vortices, although nearly equally active, are not coherent along the spanwise direction and therefore do not make a unified contribution to the spanwise average.

5.2. *Cross-stream* (y,x) *plane-averaged statistics*

In figure 17(*a*) the streamwise distribution of spanwise Kármán vortex strength, measured in terms of the (y,z) plane-average of the spanwise swirling strength defined as

$$\langle\lambda_{i,p}\rangle_{yz} = \frac{1}{2L_yL_z}\int_{-L_y}^{L_y}\int_0^{L_z}\lambda_{i,p}\,\mathrm{d}y\,\mathrm{d}z, \tag{3}$$

is plotted for both regimes H and L corresponding to the two time instants shown in figures 14 and 15. The peaks correspond to the different clockwise- and counter-clockwise-rotating spanwise vortices. The presence of strong spanwise vortices in the immediate vicinity of the normal plate is clear in regime H, whereas for regime L the first significant peak occurs only at $x \approx 2.5$. The plots if scaled by the area of cross-

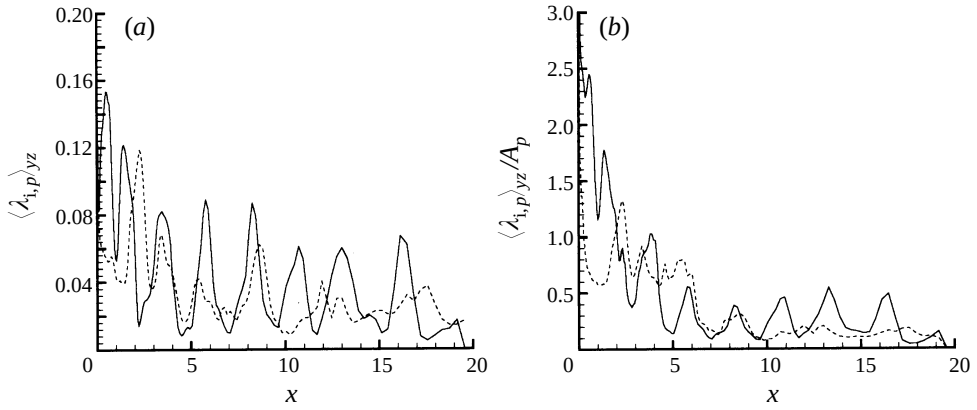

FIGURE 17 (*a*). Streamwise evolution of the instantaneous (y, z)-plane-averaged spanwise swirling strength, $\langle\lambda_{i,p}\rangle_{yz}$. This plot when scaled by the cross-sectional area of the (y, z)-plane, $2L_y L_z$, gives the total swirling strength of the Kármán vortices at any streamwise location. (*b*) As (*a*) but the plane-averaged spanwise swirling strength inversely scaled by the fractional area, A_p, occupied by the primary Kármán vortices in any (y, z)-plane, $\langle\lambda_{i,p}\rangle_{yz}/A_p$. This appropriately scaled quantity provides the true intensity or the average concentration of swirling strength within the spanwise vortices. The solid line denotes regime H ($t = 416$), and the broken line denotes regime L ($t = 456$).

section ($2L_y L_z$) provide the total spanwise swirling strength at any streamwise location. Instead, if the averaging procedure were to be restricted to only regions where spanwise vortices are present (i.e. regions where $\lambda_{i,p} > 0$; note that outside the spanwise vortex $\lambda_{i,p} = 0$) then one obtains the true intensity or the average concentration of swirling strength within the spanwise vortices. In other words, figure 17(*a*) needs to be inversely scaled by the fractional area, A_p, occupied by the spanwise Kármán vortices in any (y, z)-plane, which is defined as

$$A_p(x,t) = \frac{1}{2L_y L_z}\int_{-L_y}^{L_y}\int_{0}^{L_z} I_p(x,y,z,t)\,\mathrm{d}y\,\mathrm{d}z, \quad \text{where} \quad I_p(x,y,z,t) = \begin{cases} 1 & \text{if} \quad \lambda_{i,p} > 0 \\ 0 & \text{if} \quad \lambda_{i,p} = 0. \end{cases} \tag{4}$$

The resulting plots of $\langle\lambda_{i,p}\rangle_{yz}/A_p$, shown in figure 17(*b*) for regimes H and L, are similar to those shown in figure 17(*a*). The fractional area occupied by the spanwise vortices ranges from about 6% close to $x \approx 0$, where the spanwise vortices are compact, to about 10% farther downstream, where the spanwise vortices are more diffused. As pointed out in §4.1, in vorticity-dominated regions the swirling strength is approximately half the local vorticity. So the counter-clockwise vortex (CCR0) seen in figure 16(*a*) to just form downstream of the normal plate is centred around $x = 0.5$ and has an average non-dimensional vorticity concentration of about 5.0 at this streamwise location. The vorticity concentration at the subsequent downstream vortices decreases due to diffusive and dissipative processes. The dominant counterclockwise vortex in regime L seen in figure 16(*c*) is centred around $x = 2.5$ and the average vorticity concentration at this central streamwise location is only about 2.6.

In figure 17(*a*) the sharp peaks observed in regime H are indicative of the compactness of the spanwise vortices. In between the peaks, $\langle\lambda_{i,p}\rangle_{yz}$ reaches near zero value, thereby clearly marking a well-defined braid region in between the spanwise vortices. The distinction between the spanwise vortices and the interconnecting braid regions is somewhat less well defined in regime L, especially for $x > 10$. Owing to

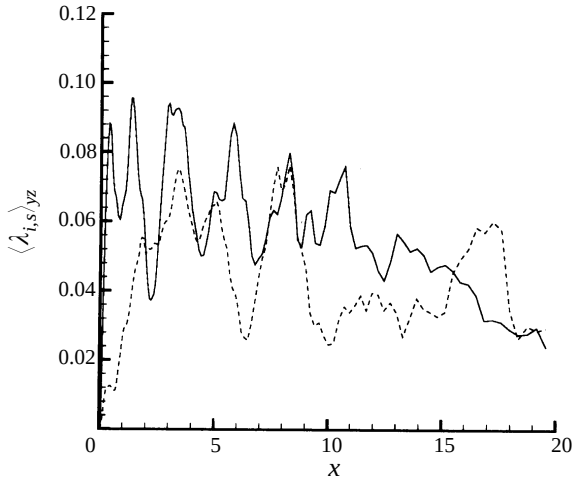

FIGURE 18. Streamwise evolution of the instantaneous (y, z)-plane-averaged cross-span (secondary) swirling strength, $\langle\lambda_{i,s}\rangle_{yz}$. Solid line denotes regime H ($t = 416$), and broken line denotes regime L ($t = 456$). This plot when scaled by the cross-sectional area of the (y, z)-plane, $2L_y L_z$, gives the total swirling strength of the streamwise vortices at any streamwise location.

tearing and spreading, the spanwise vortices are more evenly spread along the streamwise direction without a strong peak–valley structure in $\langle\lambda_{i,p}\rangle_{yz}$. In the near wake, the overall magnitude of the spanwise swirling strength is larger in regime H than in regime L, whereas the overall magnitude appears to be nearly the same farther downstream; the only difference is that the spanwise vorticity remains concentrated and focused into compact spanwise vortices in regime H, while it is more diffused in regime L. Thus some level of caution needs to be exercised in comparing figures 16(*a*) and 16(*c*). Fewer contours farther downstream in figure 16(*c*) must correctly be interpreted as lack of coherence rather than lack of spanwise vorticity.

In figure 18 the distribution of cross-span swirling strength averaged over the entire (y, z)-plane, defined as

$$\langle\lambda_{i,s}\rangle_{yz} = \frac{1}{2L_y L_z}\int_{-L_y}^{L_y}\int_{0}^{L_z}\lambda_{i,s}\,\mathrm{d}y\,\mathrm{d}z, \tag{5}$$

is plotted for both regimes H and L, corresponding to the two time instants shown in figures 14 and 15. As pointed out earlier, these plots when scaled by $2L_y L_z$ provide the total cross-span swirling strength at any streamwise location. A comparison of the regimes H and L shows that if the entire streamwise direction is taken into account, the cross-span swirling strength is about the same in both regimes. It can be observed that in regime H the x-location of peaks in the cross-span swirling strength coincide with those of peaks in the spanwise swirling strength. This may at first seem surprising since the streamwise ribs are anticipated to be most active in the braid region between the spanwise vortices. As pointed out earlier with reference to figure 16(*b*), the bending and distortion of the spanwise vortices also contribute to cross-span swirling strength. Although the concentration of swirling strength in the streamwise ribs is expected to be stronger, the streamwise ribs are spaced apart along the spanwise direction, whereas the distorted spanwise vortices occupy the entire spanwise extent. Thus the overall contribution of distorted spanwise vortices to the (y, z)-plane-averaged cross-span swirling strength, $\langle\lambda_{i,s}\rangle_{yz}$, is likely to be comparable to that from the streamwise ribs. The overlap of spanwise and cross-span swirling strengths can also be seen in regime

L, but at a much reduced level since the spanwise vortices are torn apart and distributed along the streamwise direction.

5.3. *Conditional average of cross-span swirling strength*

In order to quantify the strength of the streamwise ribs, without the inclusion of the distorted spanwise vortices, in the following we will consider the conditional average of cross-span swirling strength in regions outside the distorted spanwise vortices. In order to accomplish this, we first define a filter function $I_s(x, y, z, t)$, which will serve to isolate the streamwise ribs. The filter function will be simply defined as follows:

$$I_s(x, y, z, t) = \begin{cases} 1 & \text{if } \lambda_{i,s} > \lambda_{i,p} \quad \text{and} \quad \lambda_{i,s} > 0 \\ 0 & \text{otherwise,} \end{cases} \tag{6}$$

and $\lambda_{i,s} I_s$ will now be used to identify the streamwise ribs. In other words, the streamwise vortices are identified as regions of positive cross-span swirling strength greater than the local spanwise swirling strength. The need to separate the streamwise ribs from distorted spanwise vortices in their measurement of streamwise vorticity was originally identified by Hayakawa & Hussain (1989). In their case, the nature of the experimental measurement and the higher Reynolds number required a complex set of conditions to filter the streamwise ribs. It will be shown below that for the present case, the filter given in equation (6) will be sufficient to extract the streamwise ribs.

In figures 19(*a*), 19(*b*) and 19(*c*), contours of the three-dimensional swirling strength, $\lambda_{i,3D}$, unfiltered cross-span swirling strength, $\lambda_{i,s}$, and filtered cross-span swirling strength, $\lambda_{i,s} I_s$, are plotted on a (y, z)-plane corresponding to the streamwise location $x = 1.5$, for $t = 416$ (regime H). From figures 16(*a*) and 16(*b*), it can be seen that this plane primarily cuts through the streamwise ribs, R1, and the clockwise spanwise vortex CR0. In figure 19(*a*) the three-dimensional swirling strength can be seen to extract both the distorted spanwise vortex and the streamwise ribs which connect CR0 and CCR1. About ten streamwise vortices can be identified in this section. In the corresponding unfiltered cross-span swirling strength all of the streamwise vortices are still clearly extracted, but much of the spanwise vortex is eliminated. Some imprint of the distorted spanwise vortex can still be seen, in particular in regions where the spanwise vortex is tilted the most. Finally, in figure 19(*c*) the efficacy of the filter function (equation (6)) can be observed. The filtered cross-span swirling strength, $\lambda_{i,s} I_s$, while retaining all the streamwise ribs intact, essentially removes all of the distorted spanwise vortex. Close examination of figures 16(*a*) and 16(*b*), and also the three-dimensional visualization (figure 14), shows that the small patches of filtered cross-span swirling strength seen in figure 19(*c*) above the spanwise vortex at around $y = 0.6$ are in fact related to the downstream tips of the newly forming streamwise ribs, R0.

Based on the filter function presented in equation (6), the following two quantities are defined:

$$\langle \lambda \rangle_{rib}(x, t) = \frac{1}{2L_y L_z} \int_0^{L_z} \int_{-L_y}^{L_y} \lambda_{i,s}(x, y, z, t)\, I_s(x, y, z, t)\, \mathrm{d}y\, \mathrm{d}z, \tag{7a}$$

$$A_{rib}(x, t) = \frac{1}{2L_y L_z} \int_0^{L_z} \int_{-L_y}^{L_y} I_s(x, y, z, t)\, \mathrm{d}y\, \mathrm{d}z, \tag{7b}$$

where A_{rib} measures the fractional area on the (y, z)-plane occupied by the streamwise ribs and $\langle \lambda \rangle_{rib}$ measures the total swirling strength (inversely scaled by the area of the

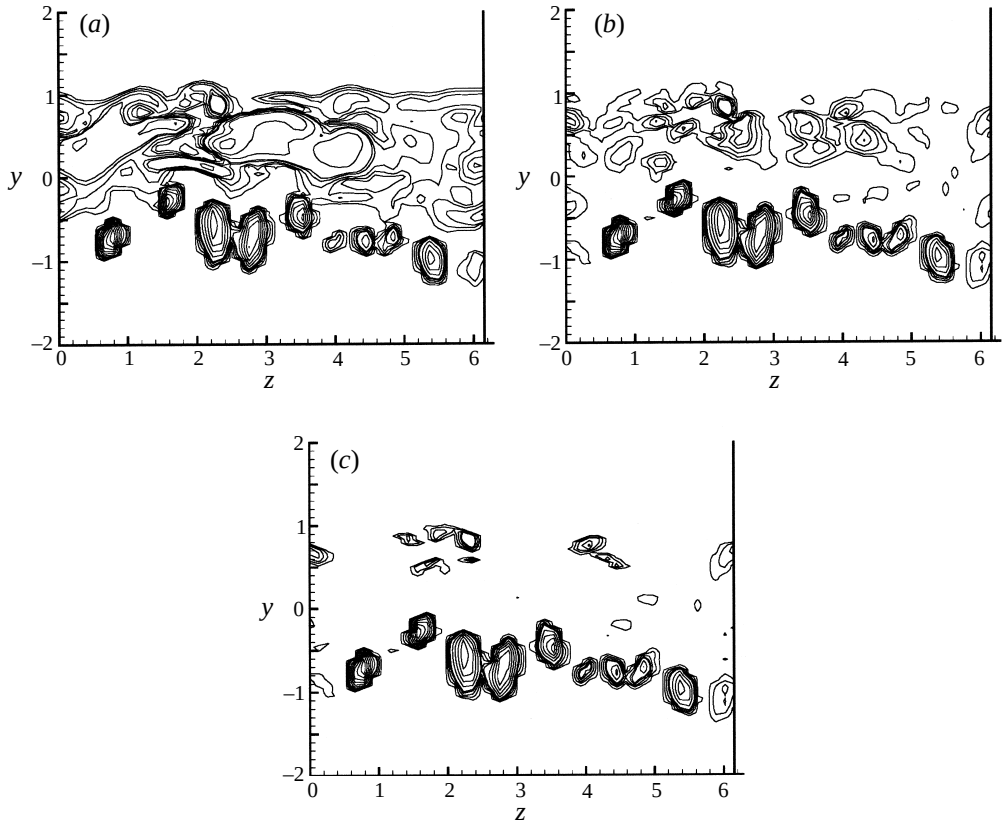

FIGURE 19. Contour plots of (*a*) three-dimensional swirling strength, $\lambda_{ci,3D}$, (*b*) unfiltered cross-span swirling strength, $\lambda_{ci,s}$, and (*c*) filtered streamwise swirling strength, $\lambda_{ci,s} I_s$, in the (y,z)-plane at $x = 1.5$ for time instant $t = 416$ (regime H). About ten streamwise ribs can be seen in all three plots, but the influence of the distorted spanwise Kármán vortex has clearly been filtered out in (*c*). Contour levels are from 0.25 to 1.75 in steps of 0.5 and from 2.0 to 9.0 in steps of 1.0.

y,z-plane, $2L_y L_z$) contained within the streamwise ribs at any streamwise location. $\langle\lambda\rangle_{rib}$ and A_{rib} can further be averaged over many different time instants covering all phases during the shedding cycle; the resulting time-averaged statistics, $(2L_y L_z \overline{\langle\lambda\rangle_{rib}}^t)$ and $\overline{A_{rib}}^t$, in regimes H and L are shown in figures 20(*a*) and 20(*b*), respectively.

In the very near wake for $x < 2.5$, the total strength of the streamwise ribs in regime H is higher than in regime L. This is understandable, since in regime L the fully rolled-up spanwise vortices form only farther downstream. In the intermediate region between $x = 2.5$ and $x = 5$, the total swirling strength of the streamwise ribs in regime L is about the same as that in regime H. Farther downstream, regime H has the larger total strength of the streamwise ribs, possibly because of the fact that the highly dispersed streamwise ribs observed in regime L undergo faster decay as they evolve downstream. The plot of fractional area of the streamwise ribs shown in figure 20(*b*) is very informative. It clearly shows that in the near-wake region, for $x < 3$, the streamwise ribs in regime L have a larger cross-sectional area consistent with their lack of spatial compactness. Farther downstream, the fractional area gradually increases downstream in both regimes suggesting diffusion of streamwise vorticity, but the fractional area of the streamwise ribs in regime H becomes larger than that in regime L. The intensity or the average concentration of swirling strength within the streamwise

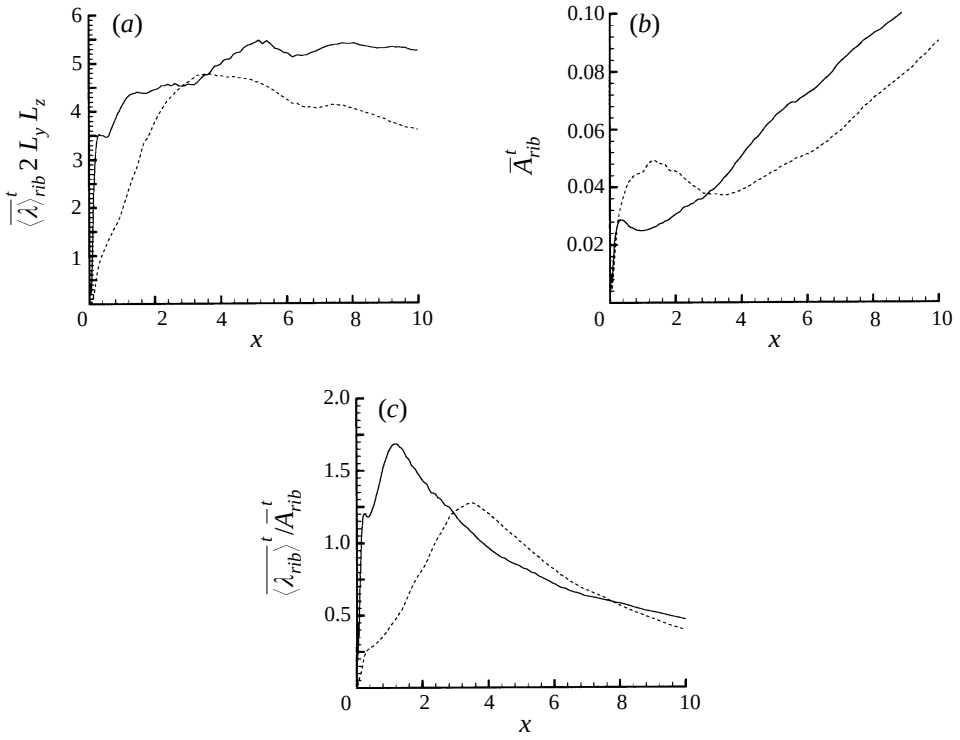

FIGURE 20. Streamwise distributions of (*a*) total swirling strength of the streamwise ribs ($2L_y L_z$) $\overline{\langle\lambda\rangle_{rib}}^t$, (*b*) fractional area, $\overline{A_{rib}}^t$, occupied by the ribs in the (y,z)-plane and (*c*) the intensity of the average concentration of swirling strength within the streamwise ribs measured as the ratio of swirling strength to the fractional area of the ribs, $\overline{\langle\lambda\rangle_{rib}}^t / \overline{A_{rib}}^t$. The solid lines denote regime H, and broken lines denote regime L. Quantities have been averaged both in the (y,z)-plane and in time.

ribs can be assessed by the following ratio: $(\overline{\langle\lambda\rangle_{rib}}^t / \overline{A_{rib}}^t)$, which is plotted for both the regimes in figure 20(*c*). The strength of the streamwise ribs is seen to peak at $x \approx 1.2$ and $x \approx 3.5$ in regimes H and L respectively and decay downstream. Figure 20(*c*) can be compared to figure 17(*b*) to gauge the relative strength of the spanwise vortices and the streamwise ribs at any streamwise location. Note that figure 17(*b*) presents an instantaneous picture, while figure 20(*c*) also involves an average over time and therefore provides a time-averaged picture. In regime L the dominant peak in figure 17(*b*) is of about the same magnitude as the peak seen figure 20(*c*), suggesting that the spanwise and streamwise vortices are of about the same average intensity. This result gives some support to the notion that in regime L the streamwise vortices have their origin in the distorted spanwise vortices. On the other hand, in regime H the peak intensity of the streamwise vortices (measured either in terms of swirling strength or in terms of vorticity) is about 60% of the dominant spanwise vortex.

6. Discussion

The characteristic three-dimensional vortex structure observed in regime H is in many ways similar to that of mode-B three-dimensional instability (Williamson 1996; Barkley & Henderson 1996; Mittal & Balachandar 1995*c*). Coherent streamwise vortices are observed and they appear to be distinct from the distorted spanwise

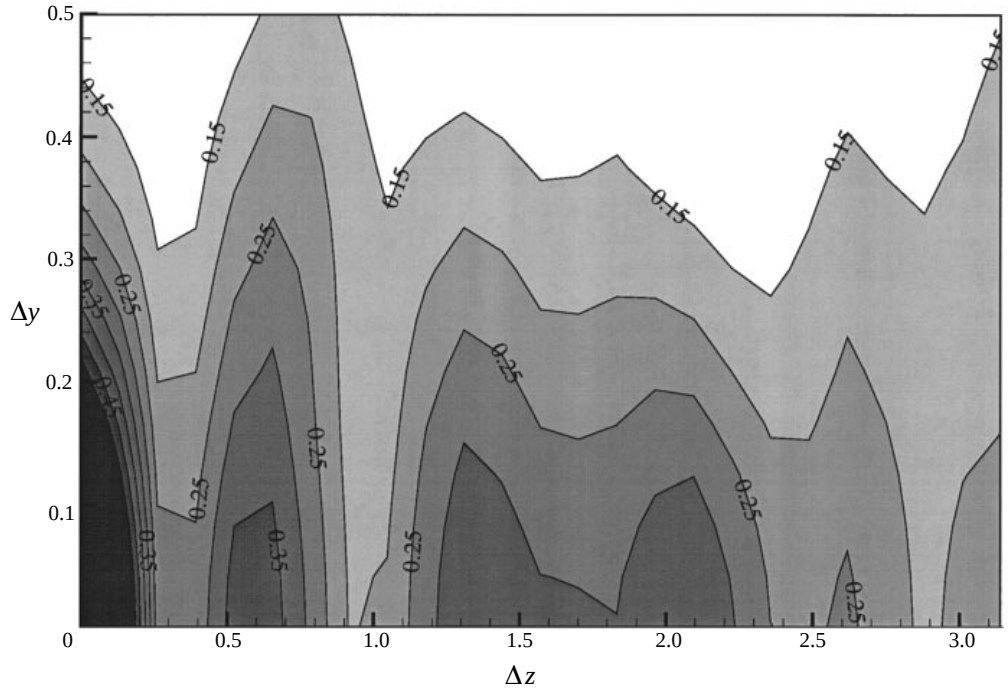

FIGURE 21. The two-point correlation, $R(\Delta y, \Delta z, t)$, of the filtered streamwise swirling strength, $\lambda_{i,s} I_s$, plotted as a function of separation along the cross-stream (y) and spanwise (z) directions, for the time instant $t = 416$, in regime H. Light shades represent low values of the correlation and dark shades correspond to high values. Contours levels are from 0.15 to 0.45 in steps of 0.05. Apart from the dominant peak at $\Delta y = 0$ and $\Delta z = 0$, a second peak at $\Delta y \approx 0$ and $\Delta z \approx 0.6$ can also be observed corresponding to a non-dimensional spanwise wavelength of about 1.2.

vortices. An estimation of the average spanwise spacing between the streamwise ribs can be obtained from a two-point correlation of the filtered cross-span swirling strength, defined as

$$R(\Delta y, \Delta z, t) = \frac{1}{2L_x L_y L_z} \times \int_0^{L_z} \int_{-L_y}^{L_y} \int_0^{L_x} \lambda_{i,s}(x, y, z, t)\, I_s(x, y, z, t)\, \lambda_{i,s}(x, y', z', t)\, I_s(x, y', z', t)\, \mathrm{d}x\, \mathrm{d}y\, \mathrm{d}z \quad (8)$$

where $y' = y + \Delta y$ and $z' = z + \Delta z$. In figure 21 the two-point correlation computed as shown above is plotted for $t = 416$ in regime H. Streamwise averaging is applied from 0 to $L_x = 2$. As can be expected there is a strong peak at $\Delta y = 0$ and $\Delta z = 0$. The second dominant peak occurs at a non-dimensional separation of $\Delta y \approx 0$ and $\Delta z \approx 0.6$, corresponding to a non-dimensional spanwise wavelength of about 1.2. This correlation peak is consistent with the five pairs of streamwise ribs seen in figures 14 and 19, which corresponds to a spanwise wavelength of $L_z/5 \approx 1.25$. This appears to be somewhat longer than the non-dimensional spanwise wavelength of the most amplified mode-B disturbance for a circular cylinder, estimated from a Floquet stability analysis to be 0.82 (Barkley & Henderson 1996). On the other hand, for a square cylinder the most amplified spanwise wavelength is estimated to be about 1.2 (Robichaux, 1997; Robichaux *et al.* 1998). Various experiments place the non-dimensional wavelength of mode-B instability for a circular cylinder to be around 1.0 over a range of Reynolds

number (Mansy, Yang & Williams 1994; Lin, Towfighi & Rockwell 1995*a*; Lin, Vorobieff & Rockwell 1995*b*; Wu *et al.* 1994; Williamson 1996; Chyu & Rockwell 1996). As can be seen from the y, z cross-sectional plots shown in figure 19, unlike in the instability modes here the ribs are not perfectly aligned along the span. Nevertheless, the correlation correctly predicts an average zero vertical displacement between the streamwise ribs.

Circulation of the streamwise vortices can be computed based on figure 20 and compared with the experimental results for mode-B shedding. From figure 20(*b*), in regime H the fractional area occupied by all the streamwise vortices at $x \approx 1$, where their intensity reaches a peak, can be estimated to be 0.026, which corresponds to a total non-dimensional area of 2.6 (since $2L_y L_z \approx 100$). With an approximate count of ten streamwise vortices, the above estimate translates to an average non-dimensional diameter of 0.575 for the streamwise vortices. This is consistent with the cross-sectional plot shown in figure 19. Note that since the (y, z)-plane is not normal to the streamwise vortices, the actual diameter and the area of cross-section of the streamwise vortices might be somewhat smaller. The cross-sectional size, along with the average cross-span swirling intensity of 1.7 at $x \approx 1$ (based on figure 20*c*), allows an estimation of the streamwise circulation of 0.28π. This estimate compares reasonably well with the PIV measurement of peak circulation of 0.46π for the mode-B streamwise ribs in the wake of a circular cylinder at $Re = 200$ (Brede, Ecklemann & Rockwell 1996). Based on the above evidence it seems reasonable to consider regime H to be dominated by mode-B three-dimensionality.

In contrast, the nature of three-dimensionality in regime L is far more complex. First, some aspects of the streamwise rib structure resemble those of regime H and therefore mode-B three-dimensionality. On the other hand, the process by which the cores of the spanwise vortices undergo large-scale deformation and become streamwise vortices is indicative of mode-A instability (Williamson 1992). Mittal & Balachandar (1995*b*) have shown that the saturated state of mode-B three-dimensionality can undergo spanwise subharmonic instability resulting in period doubling. In this subharmonic instability, a substantial portion of the spanwise vortices tears away and gets stretched in the braid region to form hairpin-like vortical structures. Certain aspects of this instability are also seen in regime L. But of more immediate relevance is the observation by Williamson (1992, 1996) that the wake transition regime, where mode-A instability gives way to mode-B instability, is marked by the coexistence of two different shedding frequencies. The higher shedding frequency is associated with a more regular three-dimensional state characterized by mode-B instability, whereas the lower shedding frequency is associated with large-scale dislocations in conjunction with either mode-A or mode-B shedding (referred to as mode A* or B* by Williamson 1996). He also observed that in a natural wake the two frequencies do not coexist at one time, but the flow intermittently swaps between the lower and higher frequencies. Regular signals interspersed with the periodic appearance of disturbed shedding cycles associated with spanwise phase incoherence have also been observed by Szepessy (1994). These observations are in total agreement with the behaviour of regimes H and L.

It therefore appears that the low-frequency unsteadiness can be characterized as the wake periodically switching back and forth between a reasonably well-organized mode-B-like three-dimensional regime and a disorganized, dispersed regime of three-dimensionality reminiscent of vortex dislocation. The key difference between these two regimes is in the level of vorticity diffusion. The importance of vorticity diffusion was addressed by Kiya & Arie (1980), who included vorticity diffusion as an external

parameter in their discrete vortex simulations. They observed that as vorticity diffusion is increased the wake remained in state I (regime L) for increasingly longer period after the start-up, but eventually transitioned to state II (regime H). This is in agreement with the present observations of coherent vs. dispersed vortical structures in regimes H and L.

The appearance of a low-frequency unsteadiness in the wake of a circular cylinder as a result of beating between closely related frequencies has been addressed by Tritton (1959), Gaster (1969, 1971), and Gerich & Eckelmann (1982). By controlling the generating of vortex dislocations with the interaction of two slightly different shedding frequencies, Williamson (1992) has observed that the dislocations can be made to occur at a regular rate and that the rate at which the dislocations are formed is determined by the beat frequency. In the present case, the average frequencies in regimes H and L are computed to be 0.162 and 0.148, respectively (see §3.3). This yields a beat frequency of 0.014, corresponding to a beat period of about 71.5, which compares reasonable well with the average low-frequency period of about 65.5 (see figure 8). Of course, the above estimation of beat frequency is only approximate. As can be seen from figure 7(*c*), there is no one single frequency that characterizes each of the regimes H and L; the shedding frequency shows a continuous variation and falls over a wide range.

For the case of a circular cylinder, clear experimental evidence indicating the coexistence of two frequencies exists only over a limited range of wake transitional Reynolds number ($180 < Re < 260$; Williamson 1996) and at much higher Reynolds number ($Re > 10^5$; Schewe 1983). Recent computational results in the transitional regime ($Re = 225$) suggest the presence of a low frequency (Belov *et al.* 1997), whereas three-dimensional numerical simulations at higher Reynolds numbers of $Re = 500$ and 1000 (Henderson 1994) do not display any significant low-frequency behaviour. Based on the above results for a circular cylinder it is tempting to conclude that the low-frequency behaviour is limited to a narrow window of Reynolds number in the wake transition regime.

For a normal plate, computational results indicate the presence of a strong low-frequency component not only at the present modest Reynolds number of 250, but also at a higher Reynolds number of 1000 (Najjar & Vanka 1995*a*). Furthermore, experimental results by Lisoski (1993) over a wide range of Reynolds number, from $Re = 1000$ to 12500, show a strong low-frequency component in the drag and lift measurements, whose character is essentially the same as that observed in the present computational results. These results seem to indicate that the low-frequency behaviour is not just limited to a narrow Reynolds number window in the wake transition regime. While the model of beat frequency between mode B and the dislocation mode (A* or B*) seems to reasonably well explain the observed low-frequency unsteadiness at low Reynolds numbers, it is not entirely clear whether the same (or at least similar beat) mechanism is operational at higher Reynolds numbers as well. The striking resemblance between the drag and lift coefficients of the present case (figure 3*b*) and those of Lisoski (figure 3*c*) lends support to the idea that the mechanism might remain the same over the entire range of Reynolds number. It then remains to be seen what two frequencies are responsible for the beat phenomenon at higher Reynolds numbers.

Next we shall consider possible physical mechanisms responsible for the periodic exchange of state between regimes H and L. The results of Rockwell & Naudascher (1979) and Rockwell & Knisely (1980) for a cavity flow have shown that the low-frequency unsteadiness has its origin in the feedback of signals from the reattachment point to the separating shear layers. This suggests a possible resonance in the absolutely unstable region of the wake. Eaton & Johnston (1982) envisioned that an

unusual event may trigger a temporary imbalance through a short-term breakdown in the spanwise vortices. The resulting decreased entrainment will lead to a temporary expansion of the recirculation region, which after a few shedding cycles will recover back to the original state. Kiya & Sasaki (1985) inferred from their detailed measurements that the low-frequency unsteadiness is associated with repeated decrease and increase in the spanwise coherence of the Kármán vortices. They further pointed out that the spanwise breakdown has a reasonably constant period and hence the feedback mechanism from the reattachment point to the separating shear layers proposed by Rockwell (1983) cannot be discounted.

Cherry *et al*. (1984) suggested that there are two different shedding phases and that the low-frequency unsteadiness is related to the relaxation process governing the change over from one phase to the other. Finally, Szepessy (1994) observed that one possible explanation for the low-frequency unsteadiness in the measured surface pressure correlation is the appearance of perturbed shedding cycles, which are marked by spanwise phase incoherence in the shedding process. All the above proposals are in reasonable agreement that the low-frequency unsteadiness can be viewed as the wake oscillating between two different regimes (or states), which are marked respectively by enhanced spanwise coherence and its breakdown.

Further insight into low-frequency unsteadiness can be obtained by exploring the alternative possibility of the flow establishing a near periodic state without oscillating back and forth between two shedding regimes. Williamson (1992, 1996) has shown that by carefully controlling the cylinder end conditions, the periodic occurrence of vortex dislocations can be avoided and a relatively periodic pure mode-B shedding can be obtained in the experiments. Corresponding computations performed at moderate Reynolds numbers under controlled conditions (Henderson & Barkley 1996 and Mittal & Balachandar 1995*c*) show that a nonlinearly saturated state of mode-B three-dimensionality is possible without any dislocations. This saturated state of mode B three-dimensional shedding is time periodic with period of oscillation only slightly different from that of the corresponding two-dimensional shedding and is devoid of any low-frequency component. The primary question will then be why the wake of a normal flat plate at $Re = 250$ does not establish a near periodic state in either regime H or regime L, but oscillates back and forth between the two regimes? In some sense, this question is intimately related to the origin of the repeated appearance of breakdown in spanwise coherence of the spanwise vortices or perturbed shedding or vortex dislocations observed by previous researchers.

Mittal & Balachandar (1995*c*) have explored in detail the process by which streamwise ribs are autogenerated in mode-B three-dimensional shedding and establish a periodic state. The previously generated streamwise vortices are observed to distort the newly forming spanwise vortices, which in turn pass this information on and result in the formation of a new generation of streamwise vortices identical to the previous generation. This autogeneration process was observed to establish a delicate balance between the spanwise distortion of the spanwise Kármán vortices and the strength and spanwise location of the streamwise vortices. Such a balance is central to the periodic evolution of a three-dimensional wake without any low-frequency component. This balance between the spanwise and streamwise vortical structures is intimately related to the balance between the entrainment and reinjection processes addressed by Eaton & Johnston (1982) and Kiya & Sasaki (1985).

A possible answer as to why low-frequency unsteadiness is observed must lie in the inability of the spanwise Kármán vortices and the associated three-dimensional streamwise vortex structure to establish a perfect balance in either regime H or in

Regime	Spanwise vortices	Streamwise vortices
L	Form farther from the base and are less coherent	Spatially distributed
I	Form farther from the base and are less coherent	Organized
H	Form closer to the base and are compact and coherent	Organized
D	Form closer to the base and are compact and coherent	Spatially distributed

TABLE 1. Qualitative characterization of the spanwise and streamwise vortical structures in the different regimes of the low-frequency cycle. Regimes H and L represent shedding cycles during which the mean drag was respectively high and low. Regimes I and D correspond to shedding periods during which the mean drag is increasing or decreasing, respectively.

regime L. If such a balance were to be attained in the three-dimensional state characteristic of regime H, then a periodic evolution of the wake, much like the saturated state of mode-B instability, would ensue. On the other hand, owing to its disorganized nature, a perfect balance in regime L cannot be expected; but the possibility of an approximate balance and a near-periodic state, without a dominant low-frequency component cannot be ruled out. In order to explore this balance between the spanwise and streamwise vortices, in addition to regimes H and L, data dumps in the intermediate transition regimes I and D, where the mean drag increases and decreases respectively, were analysed as well. A simple qualitative characterization of the spanwise and streamwise vortices in these four regimes is shown in table 1. The table provides only a simple basic characterization of the spanwise and streamwise vortices. For example, it is not implied that the spanwise vortices are of the same strength in regimes L and I or that the ribs are of the same level of organization in regimes I and H, etc.

The picture to be drawn from table 1 is as follows: in regime L the spanwise and streamwise vortices are not coherent. The incoherence in the streamwise ribs arises from the tearing of spanwise vortices. Since spanwise vortices are weak in regime L, during subsequent evolution the incoherence in the streamwise ribs decreases and they organize themselves in regime I, whereas the spanwise vortices are still relatively weak and form farther from the base. The organized ribs of regime I are not nearly as strong and therefore subsequently generated spanwise vortices are not torn apart and they remain coherent. As a result, the spanwise vortices begin to roll up closer to the normal plate, initiating regime H. During regime H, the organized streamwise vortices also grow in strength. The older-generation spanwise Kármán vortices of regime H begin to tear apart and result in a state of incoherent streamwise vortices in regime D. The effect of the incoherent streamwise ribs is still not felt in the formation of the Kármán vortices and therefore in regime D they still roll up closer to the base. Finally the incoherent streamwise vortices weaken the spanwise vortices as well and the wake returns to regime L. This scenario implies that within each shedding cycle a perfect synchronization between the spanwise and streamwise vortices does not exist. Some imbalance or phase mismatch exists between their generation mechanisms, which results in the low-frequency unsteadiness. It must be cautioned that the above scenario is only a conjecture based on the detailed visualization at various stages during the shedding process. Even at the present modest Reynolds number of 250 the wake

dynamics is far too complicated to extract a precise dynamical model. Future investigations under controlled conditions will hopefully shed light on the mechanistic details.

7. Conclusions

The wake behind a zero-thickness flat plate held normal to the flow at $Re = 250$ is observed to exhibit a low-frequency unsteadiness in addition to the primary shedding frequency corresponding to the Kármán vortices. This mechanism is clearly evident in the time history of instantaneous span-averaged drag and lift coefficients. Auto-correlations of drag and lift coefficients reveal that the non-dimensional shedding (or Strouhal) frequencies and low frequencies are 0.16 and 0.015 respectively. A time history of single-point velocity measurement reveals the shedding frequency, but the low-frequency unsteadiness is not apparent in the velocity signals. On the other hand, autocorrelations of the velocity signal extract the low-frequency behaviour accurately. Thus, the low-frequency unsteadiness is not just restricted to global measurements, it is a complex phenomenon experienced by the entire flow field.

In the case of the drag coefficient, a low-frequency component is superposed on top of oscillations at twice the shedding frequency. During the low-frequency cycle (or even roughly ten shedding cycles) the flow gradually switches back and forth between shedding cycles of high mean drag to shedding cycles of low mean drag. The high and low mean drag states of the wake are referred to as regime H and regime L. Owing to symmetry about the wake centreline, the mean lift within each shedding cycle remains nearly zero and therefore a noticeable low-frequency component is not superposed on the time series of the lift coefficient. Instead, the low frequency modulates the lift variation at the shedding frequency. In other words, the peak-to-valley variation in lift coefficient during a shedding cycle is at its highest value in regime H, and is very low in regime L. This low-frequency amplitude modulation can also be observed in the drag coefficient; a large variation in drag coefficient over a shedding cycle occurs when the mean drag is high, while the variation in drag coefficient over a shedding cycle is virtually non-existent when the mean drag is low. Apart from the amplitude modulation, the low-frequency unsteadiness modulates the shedding frequency as well. The shedding frequency increases from regime L to regime H, i.e. with increasing mean drag. Further, the variation in shedding frequency as flow goes from regime L to H seems to differ from its variation as the flow evolves from regime H to L, thus showing signs of hysteresis.

The spanwise Kármán vortices evolve differently in regimes H and L. In the high drag regime, the spanwise vortices are compact and roll up close to the back side of the normal plate. On the other hand, in regime L the spanwise vortices are less compact and their formation region extends farther away from the normal plate. As a result, the mean recirculation region in regime H is significantly shorter than that of regime L. The associated mean base suction pressure is higher in regime H, thus explaining the higher mean drag coefficient. The periodic generation of strong coherent spanwise vortices in the immediate wake of the plate in regime H translates to large-amplitude variation in drag and lift coefficients over the shedding cycle. In contrast, the less coherent spanwise vortices of regime L forming farther downstream result in no significant variation in drag and lift coefficients. The significantly different dynamics of the spanwise vortices can also explain the observed frequency modulation.

Further, the three-dimensional structure of the wake is also significantly different between regimes H and L. In the high-drag regime, reasonably well-organized

streamwise vortices (or ribs) are seen to extend in the braid region connecting the spanwise Kármán vortices. The spanwise vortices are significantly distorted along the spanwise direction as a result of the strain field induced by the streamwise vortices. In spite of their mutual interaction, the spanwise and streamwise vortices are observed to be distinct and this state of three-dimensionality resembles the mode-B shedding observed in circular and square cylinder wakes (Williamson 1996 and Robichaux *et al.* 1998). In the low-drag regime, the spanwise vortices are seen to tear apart and large sections of spanwise vorticity enter the braid region and get tilted and stretched along the streamwise direction to form streamwise vortices. In addition, few mode-B-type streamwise vortices are observed. In general the three-dimensional structure of the wake in regime L is highly incoherent and streamwise vorticity seems to be distributed over a larger region. This state of three-dimensionality resembles the large-scale dislocation addressed by Williamson (1992, 1996).

It appears that the low-frequency unsteadiness might be the result of a beat phenomenon arising from the interaction between the characteristic shedding frequencies in regimes H and L. It is also noted that for a three-dimensional wake to establish a periodic state, a balanced interplay between the spanwise and streamwise vortices is required. The streamwise vortices distort the spanwise vortices along the spanwise direction and these distortions aid the formation of next generation streamwise vortices (Mittal & Balachandar 1995*c*). Once this synchronized evolution is established with a perfect balance between the spanwise and streamwise vortices, the shedding cycle can continue for a long time without any low-frequency component. In contrast to this scenario, based on detailed visualization of flow structures we conjecture here that the formation of streamwise and spanwise vortices is not in perfect synchronization and as a result of this imbalance (or phase mismatch) the wake undergoes a low-frequency cycle. Further investigation is needed to verify this conjecture.

The work was supported jointly through a Post-doctoral fellowship from the Division of Advanced Scientific Computing (DASC) at the National Science Foundation and the National Center for Supercomputing Applications. The calculations were performed on the Thinking Machines CM-5 at the National Center for Supercomputing Applications (NCSA) at the University of Illinois, Urbana-Champaign. The support of these organizations is gratefully acknowledged. F. M. N. would like to acknowledge Professor Vanka for his continuous guidance and initial motivation in bluff body wakes and Dr D. K. Tafti for his support.

REFERENCES

Abernathy, F. H. 1962 Flow over an inclined plate. *Trans. ASME* D: *J. Basic Engng* **61**, WA-124.

Arie, M. & Rouse, H. 1956 Experiments on two-dimensional flow over a normal wall. *J. Fluid Mech.* **1**, 129.

Balachandar, S., Mittal, R. & Najjar, F. M. 1997 Properties of the mean wake recirculation region in the wakes of two-dimensional bluff bodies. *J. Fluid Mech.* **351**, 167.

Barkley, D. & Henderson, R. 1996 Three-dimensional Floquet stability analysis of the wake of a circular cylinder. *J. Fluid Mech.* **322**, 215.

Belov, A., Jameson, A. & Martinelli, L. 1997 Three-dimensional unsteady compressible flow calculations using multigrid. *AIAA Paper* 97-0433.

Berger, E. 1964 Bestimmung der hydrodynamischen Groessen einer Karmanschen wirbelstarsse aus hitzdrahtmessungen bei kleinen Reynoldsschen zahlen. *Z. Flugwiss.* **12**, 41.

Bloor, M. S. & Gerrard, J. H. 1966 Measurements on turbulent vortices in a cylinder wake. *Proc. R. Soc. Lond.* A **294**, 319.

Bradbury, L. J. S. & Moss, W. D. 1975 Pulsed wire anemometer measurements in the flow past a normal flat plate in a uniform flow and in a sheared flow. *Proc. 4th Intl Conf. Wind Effects on Building and Structures, London* (ed. K. J. Eaton), p. 485. Cambridge University Press.

Brede, M., Ecklemann, H. & Rockwell, D. 1996 On secondary vortices in the cylinder wake. *Phys. Fluids* **8**, 2117.

Cantwell, B. & Coles, D. 1983 An experimental study of entrainment and transport in the near wake of circular cylinder. *J. Fluid Mech.* **136**, 321.

Castro, I. P. 1971 Wake characteristics of two-dimensional perforated plates normal to an air-stream. *J. Fluid Mech.* **46**, 599.

Castro, I. P. & Jones, J. M. 1987 Studies in numerical computations of recirculating flows. *Intl J. Numer. Meth. Fluids* **7**, 793.

Cherry, N. J., Hillier, R. & Latour, M. P. 1984 Unsteady measurements in a separated and reattaching flow. *J. Fluid Mech.* **144**, 13.

Chong, M. S., Perry, A. E. & Cantwell, B. J. 1990 A general classification of three-dimensional flow fields. *Phys Fluids* **2**, 765.

Chua, K., Lisoski, D., Leonard, A. & Roshko, A. 1990 A numerical and experimental investigation of separated flow past an oscillating flat plate. *ASME Non-Steady Flow Symposium, Toronto, Canada*, 455. FED Vol. 92, p. 455.

Chyu, C. & Rockwell, D. 1996 Evolution of patterns of streamwise vorticity in the turbulent near wake of a circular cylinder. *J. Fluid Mech.* **320**, 117.

Corcos, G. M. & Lin, S. J. 1984 The mixing layer: deterministic models of turbulent flow. Part 2. The origin of three-dimensional motion. *J. Fluid Mech.* **139**, 67.

Dallmann, U., Hilgenstock, A., Riedelbauch, S., Schulte-Werning, B. & Vollmers, H. 1991 On the footprints of three-dimensional separated flows around blunt bodies. *AGARD CP*-494.

Dauchy, C., Dusek, J. & Fraunie, P. 1997 Primary and secondary instabilities in the wake of a cylinder with free ends. *J. Fluid Mech.* **332**, 295.

Davies, M. E. 1976 A comparison of the wake structure of a stationary and oscillating bluff body, using a conditional averaging technique. *J. Fluid Mech.* **75**, 209.

Eaton, J. K. & Johnston, J. P. 1982 Low frequency unsteadyness of a reattaching turbulent shear layer. In *Turbulent Shear Flows* (ed. L. J. S. Bradbury, F. Durst, B. E. Launder, F. W. Schmidt & J. H. Whitelaw), p. 162. Springer.

Fage, A. & Johansen, F. C. 1927 On the flow of air behind an inclined flat plate of infinite span. *British Aero. Res. Coun. Rep. Memo* 1104, p. 81.

Gaster, M. 1969 Vortex shedding from slender cones at low Reynolds numbers. *J. Fluid Mech.* **38**, 565.

Gaster, M. 1971 Vortex shedding from circular cylinders at low Reynolds numbers. *J. Fluid Mech.* **46**, 749.

Gerich, D. & Eckelmann, H. 1982 Influence of end plates and free ends on the shedding frequency of circular cylinders. *J. Fluid Mech.* **122**, 109.

Griffin, O. M. & Ramberg, S. E. 1974 The vortex street wakes of vibrating cylinders. *J. Fluid Mech.* **66**, 553.

Griffin, O. M. & Votaw, C. W. 1972 The vortex street in the wake of a vibrating cylinder. *J. Fluid Mech.* **66**, 553.

Hayakawa, M. & Hussain, F. 1989 Three-dimensionality of organized structures in a plane turbulent wake. *J. Fluid Mech.* **206**, 375.

Henderson, R. 1994 Unstructured spectral element methods: parallel algorithms and simulations. PhD Thesis, Princeton University.

Henderson, R. & Barkley, D. 1996 Secondary instability in the wake of a circular cylinder. *Phys. Fluids* **8**, 1683.

Joshi, D. S., Vanka, S. P. & Tafti, D. K. 1994 Large eddy simulation of the wake of a normal flat plate. *Boundary Layer and Free Shear Flows*. ASME-FED, vol. 184, p. 231.

Karniadakis, G. E. & Triantafyllou, G. E. 1992 Three-dimensional dynamics and transition to turbulence in the wake of bluff objects. *J. Fluid Mech.* **238**, 1.

KIYA, M. & ARIE, M. 1980 Discrete-vortex simulation of unsteady flow behind a nearly normal plate. *Bull. JSME* **23**, 1451.

KIYA, M. & MATSUMURA, M. 1988 Incoherent turbulence structure in the near wake of a normal plate. *J. Fluid Mech.* **190**, 343.

KIYA, M. & SASAKI, K. 1983 Structure of a turbulent separation bubble. *J. Fluid Mech.* **137**, 83.

KIYA, M. & SASAKI, K. 1985 Structure of large-scale vortices and unsteady reverse flow in the reattaching zone of a turbulent separation bubble. *J. Fluid Mech.* **154**, 463.

KUWAHARA, K. 1973 Numerical study of flow past an inclined flat plate by an inviscid model. *J. Phys. Soc. Japan* **35**, 1545.

LEDER, A. 1991 Dynamics of fluid mixing in separated flow. *Phys. Fluids* **3**, 1741.

LIN, J.-C., TOWFIGHI, J. & ROCKWELL, D. 1995*a* Instantaneous structure of near-wake of a cylinder: on the effect of Reynolds number. *J. Fluids Struct.* **9**, 409.

LIN, J.-C., VOROBIEFF, P. & ROCKWELL, D. 1995*b* Three-dimensional patterns of streamwise vorticity in the turbulent near-wake of a cylinder, *J. Fluids Struct.* **9**, 231.

LISOSKI, D. 1993 Nominally two-dimensional flow about a normal flat plate. PhD Thesis, California Institute of Technology, Pasadena, California.

LOWREY, P. & REYNOLDS, W. C. 1986 Numerical simulation of a spatially developing forced, plane mixing layer. *Rep.* TF-26, Department of Mechanical Engineering, Stanford University, Stanford, CA.

MANSY, H., YANG, P.-M. & WILLIAMS, D. R. 1994 Quantitative measurements of three-dimensional structures in the wake of a circular cylinder. *J. Fluid Mech.* **270**, 277.

MASKELL, E. C. 1963 A theory of the blockage effects on bluff bodies and stalled wings in a closed wind tunnel. *Aero. Res. Comm. Rep. & Memo* 3400.

MITTAL, R. & BALACHANDAR, S. 1995*a* Effects of three-dimensionality on the lift and drag of nominally two-dimensional cylinders. *Phys. Fluids* **7**, 1841.

MITTAL, R. & BALACHANDAR, S. 1995*b* Generation of streamwise vortical structure in bluff body wakes. *Phys. Rev. Lett.* **75**, 1300.

MITTAL, R. & BALACHANDAR, S. 1995*c* Autogeneration of three-dimensional vortical structures in the near wake of a circular cylinder. *TAM Rep.* 812. University of Illinois, Urbana-Champaign.

NAJJAR, F. M. 1994 Direct numerical simulations of separated and separated-reattaching flows on massively parallel processing computers. PhD Thesis, University of Illinois at Urbana-Champaign.

NAJJAR, F. M. & BALACHANDAR, S. 1996 Transition dynamics in the wake of a normal flat plate. *Bull. Am. Phys. Soc.* **41**, 1715.

NAJJAR, F. M. & BALACHANDAR, S. 1997 Low-frequency unsteadiness in the wake of a normal plate, *TAM Rep.* 860, Department of Theoretical & Applied Mechanics, University of Illinois, Urbana-Champaign.

NAJJAR, F. M. & VANKA, S. P. 1995*a* Effects of intrinsic three-dimensionality on the drag characteristics of a normal flat plate. *Phys. Fluids* **7**, 2516.

NAJJAR, F. M. & VANKA, S. P. 1995*b* Simulations of the unsteady separated flow past a normal flat plate. *Intl J. Numer. Meth. Fluids* **21**, 525.

PAULEY, L. P., MOIN, P. & REYNOLDS, W. C. 1990 The structure of two-dimensional separation. *J. Fluid Mech.* **220**, 397.

PERRY, A. E. & CHONG, M. S. 1987 A study of eddying motions and flow patterns using critical point concepts. *Ann. Rev. Fluid. Mech.* **19**, 125.

PERRY, A. E. & STEINER, T. R. 1987 Large-scale vortex structures in turbulent wakes behind bluff bodies. Part 1. Vortex formation processes. *J. Fluid Mech.* **174**, 233.

PIERREHUMBERT, R. & WINDALL, S. 1982 The two- and three-dimensional instabilities of a spatially periodic shear layer. *J. Fluid Mech.* **114**, 59.

PRASAD, A. & WILLIAMSON, C. H. K. 1997 The instability of the shear layer separating from a bluff body. *J. Fluid Mech.* **333**, 375.

REYNOLDS, W. C. & HUSSAIN, A. K. M. F. 1972 The mechanisms of an organized wave in turbulent shear flow. Part 3. Theoretical models and comparisons with experiments. *J. Fluid Mech.* **54**, 263.

ROBICHAUX, J. 1997 Study of three-dimensional vortex shedding in the wake of a square cylinder. PhD. thesis, University of Illinois at Urbana-Champaign.

ROBICHAUX, J., BALACHANDAR, S. & VANKA, S. P. 1998 Three-dimensional instability of the wake of a square cylinder. *Phys. Fluids* (accepted).

ROCKWELL, D. 1983 Oscillations of impinging shear layers. *AIAA J.* **21**, 645.

ROCKWELL, D. & KNISELY, C. 1980 Vortex edge interaction mechanisms for generating low frequency components. *Phys. Fluids* **23**, 239.

ROCKWELL, D. & NAUDASCHER, E. 1979 Self-sustained oscillations of impinging free shear layers. *Ann. Rev. Fluid Mech.* **11**, 67.

ROSHKO, A. 1954 On the drag and shedding frequency of two-dimensional bluff bodies. *NACA Tech. Note* 3169.

SCHEWE, G. 1983 On the force fluctuations acting on a circular cylinder in crossflow from subcritical up to transcritical Reynolds numbers. *J. Fluid Mech.* **133**, 265.

STEINER, T. R. & PERRY, A. E. 1987 Large-scale structures in the turbulent wakes behind bluff bodies. Part 2. Far-wake structures. *J. Fluid Mech.* **174**, 271.

SZEPESSY, S. 1994 On the spanwise correlation of vortex shedding from a circular cylinder at high subcritical Reynolds number. *Phys. Fluids* **6**, 2406.

SZEPESSY, S. & BEARMAN, P. 1992 Aspect ratio and end plate effects on vortex shedding from a circular cylinder. *J. Fluid Mech.* **234**, 191.

TAMURA, T., OHTA, I. & KUWAHARA, K. 1990 On the reliability of two-dimensional simulation for unsteady flows around a circular-type structure. *J. Wind Engng Ind. Aero.* **35**, 275.

TRITTON, D. J. 1959 Experiments on the flow past a circular cylinder at low Reynolds numbers. *J. Fluid Mech.* **6**, 547.

WALEFFE, F. 1990 On the three-dimensional instability of strained vortices. *Phys. Fluids* A **2**, 76.

WILLIAMSON, C. H. K. 1992 The natural and forced formation of spot-like 'vortex dislocations' in the transition of a wake. *J. Fluid Mech.* **243**, 393.

WILLIAMSON, C. H. K. 1996 Three-dimensional wake transition. *J. Fluid Mech.* **328**, 345.

WU, J., SHERIDAN, J., WELSH, M. C., HOURIGAN, K. & THOMPSON, M. 1994 Longitudinal vortex structures in a cylinder wake. *Phys. Fluids* **6**, 2883.

ZHANG, L., BALACHANDAR, S. & TAFTI, D. 1997 Effects of intrinsic three dimensionality on heat transfer and friction loss in a periodic array of parallel plates. *Numer. Heat Transfer* A **31**, 327.

ZHOU, J., ADRIAN, R. J., BALACHANDAR, S. & KENDALL, T. M. 1997 Mechanisms for generating coherent packet of hairpin vortices in near-wall turbulence. *J. Fluid Mech.* (accepted).